ROYAL SOCIETY
OF **CHEMISTRY**

REVIEW ARTICLE
Zhefeng Xu, Yueming Li *et al.*
Recent progress in 2D inorganic non-conductive materials
for alkali metal-based batteries

REVIEW ARTICLE

Check for updates

Recent progress in 2D inorganic non-conductive materials for alkali metal-based batteries

Yuxi Shen, (ID) Zengquan Zhu, (ID) Zhefeng Xu (ID) * and Yueming Li (ID) *

The urgent need for new energy storage devices has promoted studies on alkaline metal-based batteries with high energy density and long life. In this case, two-dimensional (2D) inorganic non-conductive materials have exhibited unique physicochemical properties, making them ideal candidates for energy storage and conversion owing to their planar structure, high surface-to-volume ratio, and non-electronic conductive nature. Among the 2D inorganic non-conductive materials, hexagonal boron nitride (h-BN), graphitic nitride (g-C_3N_4), montmorillonite (MMT), and vermiculite (VMT) have shown potential application in alkaline metal-based batteries. Herein, the strategies developed for the synthesis of these inorganic two-dimensional non-conductive materials in recent years and their applications as electrode material additives, metal anode supports, and building blocks of solid interfacial and separator additives in alkali metal-based batteries are comprehensively reviewed. Subsequently, challenges associated with the use of 2D materials in alkali metal-based batteries to improve their performance are discussed and possible solutions are proposed. These 2D inorganic non-conductive materials have potential to be widely used in alkali-based batteries in the future considering their unique structure and properties.

1. Introduction

Presently, the development of renewable energy has become necessary to address the energy crisis and environmental pollution. However, the instability and volatility of renewable energy sources create a significant challenge in terms of energy storage. In this case, rechargeable batteries are widely employed to store renewable energy and bridge the gap between supply and demand.[1] Among them, lithium-ion batteries (LIBs) as a type of alkali metal-based battery have emerged as one of the most commonly used energy storage solutions due to their high energy density, long cycle life, and low self-discharge rate. Nevertheless, with the rapid development of electric vehicles and portable electronic devices, the demand for batteries with higher energy density and extended driving range has grown, pushing traditional LIBs close to their limit. Consequently, researchers have shifted their attention to next-generation battery technologies with higher theoretical energy densities.

Besides LIBs, other alkali metal-based batteries such as Li–metal, Li/Na–O_2, Li–S, and Na/K metal batteries have attracted significant attention due to their higher specific capacity and lower costs. Lithium metal batteries (LMBs) have received significant

research and exploration, in which lithium metal is used as the anode material, offering a higher theoretical energy density. As is known, lithium metal is lightweight (0.59 g cm^{-3}) and possesses a low reduction potential (−3.04 V *vs.* the standard hydrogen electrode) and high theoretical specific capacity (3860 mA h g^{-1}). However, LMBs encounter multiple challenges such as lithium dendrite formation and electrolyte decomposition, requiring necessary improvements for their practical application.[2] In this case, another promising type of alkaline-based battery is lithium–sulfur (Li–S) batteries[3] because of the high theoretical capacity and abundant resources of sulfur element. However, Li–S batteries are also associated with challenges such as the shuttle of polysulfides and low conductivity of the S element, which need to be addressed to achieve reliable commercialization. Additionally, lithium–oxygen (Li–O_2) batteries (LOBs) are considered potential high-energy-density energy storage devices.[4] LOBs utilize oxygen gas as the active cathode material, enabling a higher theoretical energy density. However, LOBs are associated with challenges related to the formation of solid oxide byproducts and the poor catalytic efficiency of the oxygen electrode. Also, besides the scientific issues, the large-scale application of lithium-based batteries is restricted by the limited and uneven distribution of lithium reserves. Thus, to overcome these issues, researchers have begun to study sodium-ion batteries (SIBs)[5,6] and potassium-ion batteries (PIBs)[7] as cost-effective alternatives to LIBs. Sodium and potassium elements with rich resources exhibit similar chemical properties and ion transport mechanisms, making them potential substitutes for LIBs.

State Key Laboratory of Metastable Materials Science and Technology, College of Materials Science and Engineering, Yanshan University, Qinhuangdao 066004, China. E-mail: zfxu@ysu.edu.cn, liyueming@ysu.edu.cn

However, SIBs exhibit poor kinetic characteristics due to the insertion of the Na ion with a larger radius into the host structure, which can result in the degradation of the host material. In addition, the lower Lewis acidity of sodium complexes leads to the higher solubility of the solid–electrolyte interphase (SEI), which can result in incomplete coverage of the electrode surface and some detrimental side reactions, accelerating the generation of heat. Furthermore, the currently used cathode materials, including oxides, poly-anions, organics, and Prussian blue and its analogs, all suffer from poor electronic/ion conductivity.[5] In addition, although the use of sodium metal as the anode can solve the issues of poor kinetic insertion of Na^+ ions and low capacity, it encounters a similar dilemma as the lithium metal anode. Specifically, during the cycling process, the reaction between sodium metal and the electrolyte continuously increases the interface impedance and consumes the electrolyte, leading to a continuous decrease in the Coulombic efficiency during the charge–discharge process. Furthermore, the formation of a large number of sodium dendrites on the anode surface and generation of "dead sodium" also reduce the cycling stability. Also, the further growth of sodium dendrites may penetrate the separator, leading to short circuits and even explosions.[8]

Potassium possesses a standard hydrogen electrode potential (-2.936 V $vs.$ SHE) between that of lithium and sodium. Additionally, potassium ions have smaller solvation shells compared to lithium and sodium ions, resulting in higher ionic conductivity and solubility. However, given that research in this field is still in its infancy, potassium-ion batteries encounter similar challenges as SIBs. The insertion of larger potassium ions causes more significant volume changes in the electrode materials during the charge–discharge processes compared to other alkali metal ion batteries, leading to unstable electrode structures.[7,9] Additionally, the low diffusion rate of K^+ in solid electrode materials limits its rate performance. Similarly, the lower potential and higher capacity of potassium metal make it an attractive candidate as a negative electrode for potassium batteries. However, potassium metal electrodes also encounter dendritic growth. Furthermore, the incompatibility of K metal and the standard copper foil current collectors presents another significant obstacle in the development of PIBs.[10] In this case, studies have shown that modification of the electrode materials is very helpful in addressing the issues in these batteries.

As is known, inorganic materials play a critical role in alkaline metal-based batteries. For example, the common commercial LIBs use graphite as the anode and $LiNi_xCo_yMn_z$ as the cathode. Some inorganic materials have been shown to play a unique role in alkali metal/ion batteries. For example, sodium trisilicate can be used as an electrode binder to produce rigid, load-bearing batteries due to its high strength and stiffness.[11]

Two-dimensional (2D) inorganic non-conductive materials with unique properties are expected to become one of the key materials in improving the performance of batteries. 2D inorganic materials can be divided into conductive materials, semi-conductive materials, and insulators based on their
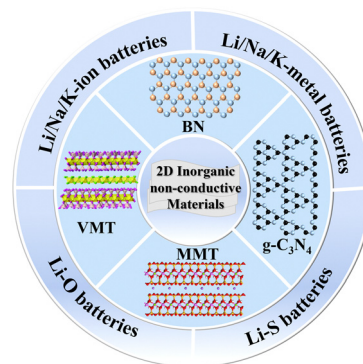

Fig. 1 Schematic diagram of the structure of representative 2D inorganic non-conductive materials and their application in various alkali metal-based batteries.

electronic conductivity. The representative examples of conductive 2D inorganic materials include graphene, MXenes ($M_{n+1}AX_n$),[12] and black phosphorus (BP) nanosheets. However, sometimes it is fussy to distinguish between insulators and wide-gap semiconductors, and thus these materials can be classified as non-conductive materials. There are also various inorganic non-conductive 2D materials such as metal hydroxides,[13] BN,[14] graphitic carbon nitride (C_3N_4),[15] MMT, and VMT.[16]

In fact, non-conductive 2D inorganic materials can play significant roles as additives for the SEI, separator, and electrolyte. To date, although the synthesis of non-conductive 2D nanosheets has been summarized in previous reports,[14,17–19] there are few reviews on the recent progress of 2D non-conductive inorganic materials as functional additives in alkali metal-based batteries.

Herein, we provide an overview of the typical 2D inorganic non-conductive materials, including BN, g-C_3N_4, MMT, and VMT developed in recent years and their application in alkali metal-based batteries. Subsequently, we briefly discuss their synthesis and fundamental properties. Finally, we emphasize their applications in alkali metal-based batteries, such as Li/Na/K-ion batteries, Li/Na/K-metal batteries, and Li–S/O batteries, as shown in Fig. 1.

2. Overview of 2D inorganic non-conductive materials

2.1. Basic properties of representative 2D materials

2D inorganic non-conductive materials are a class of nanomaterials with ultrathin thickness and very large lateral size. Their unique geometric structures endow them with unique merits including large specific surface area, short diffusion path for carrier ions, and rich surface chemistry. Additionally, their interlayer covalent bonds in 2D planes ensure adequate mechanical strength. 2D materials can be prepared via the exfoliation of layered materials. Also, 2D inorganic non-conductive materials can be used as building blocks for other micro/nano structures, making them suitable to be applied in

various energy storage fields. Furthermore, the wide bandgap of 2D inorganic non-conductive materials makes them favourable as key components in the passivation layer.

2.1.1 Basic properties of hexagonal BN. Boron nitride exists as multiple allotropes, and among them, hexagonal boron nitride (h-BN) and cubic boron nitride (c-BN) are the most stable.[20] h-BN is a layered hexagonal crystal, with a structure analogous to graphite. It belongs to the $P6_3/mmc$ space group, with lattice parameters of a = 2.505 Å and c = 6.653 Å. The B and N atoms are bonded through in-plane connections, forming a hexagonal lattice, and multiple layers stack to create large h-BN crystals.[21] Due to the sp^2 bonding in h-BN, the B–N bonds within the plane exhibit remarkable in-plane thermal conductivity, chemical stability, and strength. Also, due to the layered structure of h-BN bulk materials, they can be exfoliated into BN nanosheets. The bulk modulus of a single layer of h-BN is approximately 160 GPa, while its bending modulus is around 31.2 GPa. The presence of empty π orbitals in h-BN makes it an electrical insulator, with an energy bandgap of approximately 5.955 eV.[21–23] The ionic nature of the B–N bonds results in layer-to-layer interactions, leading to an AA′ stacking configuration, where each N atom is directly above the B atoms of the subsequent layer. In addition to AA′ stacking, energetically higher AB stacking (Bernal stacking) is occasionally observed in thin h-BN films.[24–27]

The unique structure of BN is responsible for its unique properties such as high chemical stability, strong mechanical strength, special optical properties, and special optoelectronic properties.

2.1.2 Basic properties of g-C₃N₄. Graphitic carbon nitride (g-C₃N₄) exhibits a planar two-dimensional layered structure resembling graphene, with carbon and nitrogen atoms in an sp^2 conjugated configuration, forming a hexagonal structure, as shown in Fig. 2.[28] This structure consisting of six atoms is referred to as a triazine ring. Each triazine ring is linked to an adjacent unit through C–N bonds. Currently, it is widely believed that g-C₃N₄ may have one of two chemical frameworks, *i.e.*, g-CN with triazine rings (C₃N₃), which is a part of the R_3m space group, or g-CN with 3-s-triazine rings (C₆N₇), which is a part of the $P6m^2$ space cluster.[29] Within g-C₃N₄, each triazine ring is connected to another ring *via* a terminal nitrogen ion, resulting in a homogeneous structure capable of infinite growth. Subsequent experimental and computational analyses have indicated that g-C₃N₄ composed of triazine rings as the fundamental unit is more stable than the structure composed of 3-s-triazine rings. During the preparation of g-C₃N₄, it can be controllably adjusted to adopt 0D, 1D, 2D, and 3D morphologies.[30] Generally, 0D-structured g-C₃N₄ exhibits significant size quantization effects, surface effects, and quantum confinement effects. In the case of 1D-structured g-C₃N₄ (mainly nanotubes and nanofibers), it provides a direct pathway for electron transfer. Alternatively, the interconnected structure of 3D g-C₃N₄ results in good porous channels, rapid electron transfer, larger specific surface area, and more active sites. Additionally, the two surfaces of its two-dimensional nanosheets possess expansive specific surface areas and abundant exposed surface sites.[31] Also, due to the unique structure of g-C₃N₄, it displays tunable optoelectronic properties.[32]

2.1.3 Clay-based 2D materials. Montmorillonite (MMT) belongs to the natural smectite group, which is a silicate mineral with a layered structure and high mechanical properties, as shown in Fig. 2(e).[36] Its composition can be expressed as [(Na,Ca)₀.₃₃ (Al, Mg)₂(Si₄O₁₀) (OH)₂·nH₂O]. The basic molecular structure of MMT is composed of silica tetrahedra and aluminum octahedral units. The Si⁴⁺ cation has tetrahedral coordination with oxygen, while the Al³⁺ cation has six-fold or octahedral coordination with oxygen.[37] MMT consists of two layers of O–Si–O tetrahedral silicate sheets sandwiching an alumina layer, forming a 2 : 1 clay with O–Al (Mg)–O octahedral sheets. The silica layers form a hexagonal network by sharing three corners with adjacent tetrahedra.[38] The remaining fourth corner of each tetrahedron is connected to adjacent octahedral sheets. Aluminum or magnesium, coordinated with oxygen and hydroxyl groups from the tetrahedral layer, form octahedral layers. With the help of van der Waals and electrostatic forces, or through hydrogen bonding, neighboring layers of approximately 10 μm in size stack to form the basic particles of MMT.[39] Additionally, the isomorphous substitution of some of the Al³⁺ in the octahedral sheets with divalent metal cations such as Mg²⁺ and Fe²⁺ or other lower charge cations leads to charge deficiency in the MMT layers. In this case, to balance the charge deficiency, interlayer cations can be exchanged with other metal cations.[40,41]

Vermiculite (VMT) is a common layered silicate mineral that is characterized by natural, non-toxic, high expansion, and load-bearing properties. It is the primary product from the low-temperature hydrothermal treatment of biotite and phlogopite micas.[42,43] VMT is formed by the progressive transformation of the original mica. Monolayer VMT has a typical 2 : 1 structure, composed of two layers of silicon–oxygen tetrahedra sandwiching a layer of magnesium–oxygen octahedral,
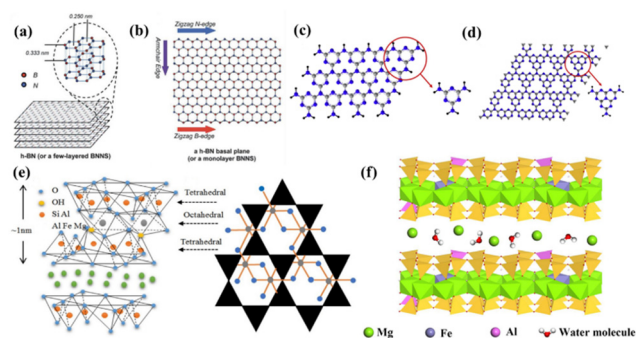
Fig. 2 (a) Layered van der Waals structure of bulk h-BN and (b) planar view of an atomically thin sheet of sp^2-bonded B and N atoms that comprise the h-BN crystal or BN nanosheets (BNNS). Adapted with permission.[33] Copyright 2012, The Royal Society of Chemistry. Stacking 2D layering composition and fundamental constituent elements of (c) s-triazine and (d) tri-s-triazine of g-C₃N₄.[34] Copyright 2017, Elsevier. (e) Schematic representation of the structure of MMT.[35] Copyright 2021, Multidisciplinary Digital Publishing Institute. (f) Schematic diagram of VMT structure.[19] Copyright 2021, Elsevier.

as shown in Fig. 2(f).[44] The thickness of monolayer VMT is approximately 1 nm, with an interlayer spacing of about 1.4 nm.[20] Due to the substitution of aluminum for a portion of silicon in the silicate layers, VMT layers carry a negative charge.[45] Therefore, there are numerous cations, such as K^+, Mg^{2+}, and Ca^{2+}, present in the interlayer space of VMT to maintain charge balance.[45,46] VMT exhibits a unique characteristic of volume expansion upon heating at elevated temperatures.[47] Expanded VMT possesses excellent properties such as light weight, low thermal conductivity, insulation, sound absorption, and adsorption.[19,48] Furthermore, delaminated VMT nanosheets have a larger specific surface area than expanded VMT due to their exposed interlayer surfaces after delamination.[49–53] Thus, the fresh surface of delaminated VMT nanosheets possesses abundant reactive sites, contributing to significantly higher reactivity compared to expanded VMT. Moreover, VMT nanosheets exhibit a high concentration of negative charges on their surfaces, providing excellent electrical conductivity compared to expanded VMT.[54]

A single layer of VMT has a typical 2 : 1 structure, which consists of two layers of silicon oxygen tetrahedra sandwiched by a layer of magnesium oxygen octahedra. There are many cations, such as K^+, Mg^{2+}, and Ca^{2+}, in the interlayer of VMT to maintain electrical balance.[19]

2.2. Methods for the preparation of 2D non-conductive materials

2.2.1 Synthesis of BN nanosheets.
Several methods have been developed to prepare h-BN nanosheets. These methods can be divided into two categories, top–down process and bottom–up process. Top–down processes mainly include liquid phase exfoliation and mechanical exfoliation, while bottom–up processes include physical vapor deposition, solvothermal synthesis, laser plasma deposition, chemical vapor deposition, vapor–liquid–solid growth, and molecular beam epitaxy growth.[20] The detailed synthesis methods have been introduced in previous reports. The typical bottom–up process for the growth of h-BN involves initial annealing and treatment of the substrate/catalyst, followed by exposure to precursors containing B and N compounds at high temperatures. The catalytic substrate promotes the decomposition of the surface precursors and the nucleation and growth of h-BN.[27,55–70] For example, h-BN can be directly grown on SiO_2 substrates using low-pressure chemical vapor deposition (LPCVD) with solid ammonia borane precursors or Ru (0001) surface *via* the CVD method, resulting in the formation of h-BN films with thicknesses of dozens of nanometers (Fig. 3(a)–(c)).[71–74]

2.2.2 Synthesis of g-C_3N_4.
Similar to h-BN, both the top–down and bottom–up approaches can be applied to prepare 2D g-C_3N_4. Several methods including the template method, sol–gel method, and exfoliation method can be used to prepare graphitic carbon nitride. Wang *et al.*[77] summarized the recent advances in the preparation and environmental application of g-C_3N_4-based materials. The preparation of g-C_3N_4 nanoparticles (NPs) involves the convection heating of various N-containing organic compounds, including melamine, urea,
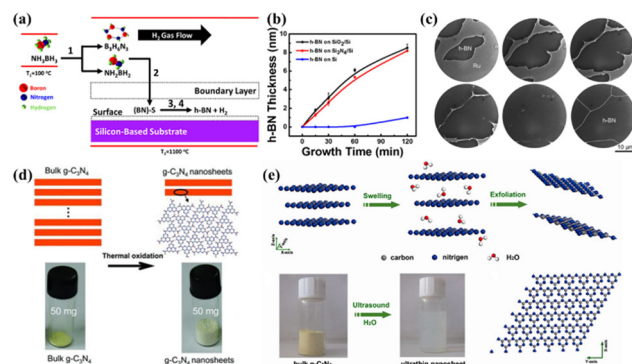
Fig. 3 (a) Schematic of h-BN growth process. (b) Variation in h-BN film thickness at different CVD growth times for Si_3N_4/Si, SiO_2/Si, and Si substrates.[72] Copyright 2017, the American Chemical Society. (c) LEEM images of different stages of h-BN growth on Ru(0001) *via* CVD.[73] Copyright 2011, the American Chemical Society. (d) Schematic of the structures of bulk g-C_3N_4 and the g-C_3N_4 nanosheets. A volume comparison of 50 mg powder of bulk g-C_3N_4 and g-C_3N_4 nanosheets is given.[75] Copyright 2012, Wiley-VCH. (e) Schematic diagram of preparation, physical image, and perfect crystal structure of g-C_3N_4.[76] Copyright 2012, the American Chemical Society.

thiourea, cyanamide, and dicyandiamide.[30,75,78–86] The top–down approach utilizes methods such as thermal oxidation, ultrasonic treatment, and chemical etching to exfoliate g-C_3N_4 into ultrathin sheets. The bottom–up approach involves the direct synthesis of g-C_3N_4 nanosheets using nitrogen-rich precursors, templates, or intermolecular interactions.[75] An example of the top–down method is shown in Fig. 3(d), where Niu *et al.*[85] prepared g-C_3N_4 *via* the exfoliation of bulk g-C_3N_4 employing thermal oxidation. The top–down approach enables the exfoliation of bulk materials into g-C_3N_4 nanosheets, but it should be noted that the thinnest material does not necessarily guarantee the best performance.[84] In the case of the bottom–up approach, Kang *et al.*[86] prepared highly dispersed g-C_3N_4 nanosheets with a thickness of approximately 2–3 nm *via* the direct *in situ* thermal decomposition of NH_4HSO_4 and melamine in air.[76] Additionally, Zhang *et al.*[87] for the first time prepared ultrathin graphite-like C_3N_4 (g-C_3N_4) nanosheets from bulk g-C_3N_4 in water *via* a "green" liquid exfoliation route. The resulting ultrathin g-C_3N_4 nanosheet solution was highly stable in acidic and alkaline environments and exhibited pH-dependent photoluminescence (PL) (Fig. 3(e)).

2.2.3 Synthesis of 2D clay nanosheets

2.2.3.1 Synthesis of 2D MMT. According to the previous discussion, it is known that the interlayer cations of MMT can be exchanged with other metal/organic cations. Also, ion exchange is the most commonly applied modification method to prepare 2D MMT nanosheets. For example, Yang *et al.*[88] prepared lithium-intercalated MMT (Li-MMT) by adding commercial calcium-based MMT and Li_2CO_3 to distilled water, as shown in Fig. 4(a). Hu *et al.*[89] employed a similar method to modify sodium-based MMT with hexadecyltrimethylammonium bromide (CTAB) to obtain CTAB-MMT, as shown in Fig. 4(b). Specifically, during the pretreatment of the original MMT, the slurry was first subjected to low-speed centrifugation,
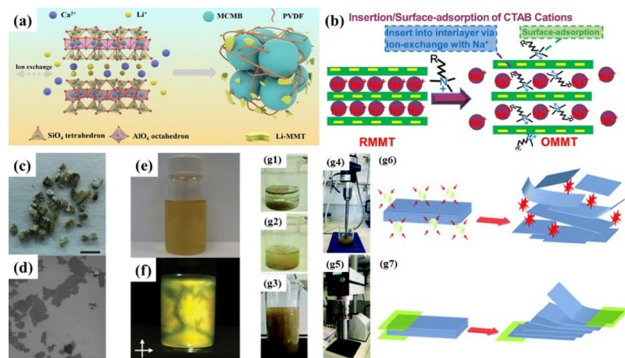
Fig. 4 (a) Schematic illustration of the synergistic protection of MCMB by Li-MMT and PVDF.[88] Copyright 2022, The Royal Society of Chemistry. (b) Schematic of insertion/surface-adsorption of CTAB cations in OMMT.[89] Copyright 2022, Elsevier. (c) Thermally expanded vermiculite crystals (scale bar, 5 mm), which can be exfoliated by ion exchange to form (d) nanosheets, SEM image (scale bar, 50 nm). (e) Single to few-layer dispersion in water. (f) Dispersion exhibits strong birefringence when viewed through crossed polarizers, suggesting nematic ordering originating from the high aspect ratios of the flakes.[51] Copyright 2015, Springer Nature. (g) Physical and schematic diagram of ultrasonic and shear force preparation of expanded vermiculite.[92] Copyright 2018, The Royal Society of Chemistry.

and then the upper suspension was centrifuged further at high speed to obtain thinner MMT flakes. Using this ion exchange strategy, carbon intercalated[90] and FeS$_2$ intercalated MMT[91] could be prepared.

2.2.3.2 Synthesis of 2D VMT nanosheets. VMT is a type of natural hydrate clay mineral, which is composed of multiple-lamella (silicon–oxygen tetrahedron) and intercalated ions.[93] These 2D nanosheets form three-dimensional structures through weak interlayer interactions such as hydrogen bonds and van der Waals forces.[50] Therefore, by weakening the interlayer interactions in the VMT interlayer space and increasing the interlayer spacing, VMT can be exfoliated into two-dimensional nanosheets.[94] Thus, there is a close relationship between the expansion and exfoliation mechanisms of VMT.

The difference between VMT exfoliation and expansion primarily lies in the degree of weakening of the interlayer interactions in VMT. When the interlayer interactions are weakened to a certain extent, VMT undergoes exfoliation. VMT can be exfoliated into monolayer nanosheets with diameters ranging from tens to hundreds of nanometers. Furthermore, the thickness of VMT nanosheets typically consists of only a few atomic layers.[92] The general approaches for preparing exfoliated VMT nanosheets include chemical treatment, mechanical treatment, and a combination of both methods.[51] Fig. 4c–g show the two typical examples of the preparation of 2D VMT nanosheets.[95]

3. 2D inorganic materials in alkali metal-based batteries

3.1. Application of h-BN in alkali metal-based batteries

The 2D non-conductive materials can hardly be used as electrode materials directly due to their poor electron transfer capability. However, they can be used as additives in electrode materials, separators, and electrolytes because of their unique structure. Given that batteries are complex systems composed of multiple components including electrode materials, electrolytes, separators, and SEI layer, modification of their individual component is expected to effectively enhance their overall performance. On one hand, conductive 2D inorganic materials can significantly enhance the electrochemical performance of electrode materials. On the other hand, the components in batteries such as separators and SEI layers require materials with non-conductive properties. Goodenough *et al.*[96] proposed that the stable window of the electrolyte can be evaluated using the following equation.

$$E_g = E_{LUMO} - E_{HOMO}.$$

(where E_{LUMO} and E_{HOMO} correspond to the voltages of the lowest unoccupied molecular orbital (LUMO) and the highest occupied molecular orbital (HOMO) of the electrolyte, respectively.) When the chemical potential of the anode (μ_a) is greater than E_{LUMO} ($\mu_a > E_{LUMO}$), electrons tend to transfer from the anode to the electrolyte LUMO conduction band, thereby reducing E_{LUMO}, which widens the stable window of the electrolyte. Additionally, the formation of an SEI layer on the negative electrode can extend the stable window, but its formation of results in irreversible lithium consumption. Therefore, pre-assembling an artificial SEI layer on the negative electrode of the battery can effectively widen the stable window of the electrolyte and reduce the irreversible lithium consumption during the formation of the SEI layer. Additionally, the separator, as a crucial component of the battery, serves to isolate the cathode and anode while containing the electrolyte, thus facilitating ion transport. The failure of the membrane can have severe consequences for the battery.

Separators play a vital role in batteries. The separator should possess the following characteristics to ensure the proper operation of batteries: (1) excellent chemical stability and compatibility to prevent reactions with other battery components and ensure compatibility with the electrolyte; (2) outstanding mechanical strength to maintain the integrity of the separator and prevent dendrite penetration; (3) good thermal stability to avoid significant shrinkage at high temperatures, and (4) good ion permeability to facilitate rapid ion transport. The thermal stability of commercial PP or PE separators should be further enhanced, and thus coating inorganic materials on the surface of these separators has been proven an effective method to improve their thermal stability.[97]

3.1.1 Alkali-ion batteries

3.1.1.1 Electrode material additives. As the extensively used and commercially available alkali batteries, LIBs mainly use graphite as the anode, but it suffers from a lack of safety and a low theoretical capacity. In this case, graphene nanosheets can act as anode materials with a higher capacity in LIBs; however, their cycling stability is poor. Li *et al.*[98] prepared reduced graphene oxide (rGO)/nitride boron thin films through simple vacuum filtration followed by thermal treatment (Fig. 5(a)). Due to the unique structure of the rGO/h-BN thin films and the synergistic effect between the layered BN and graphene,
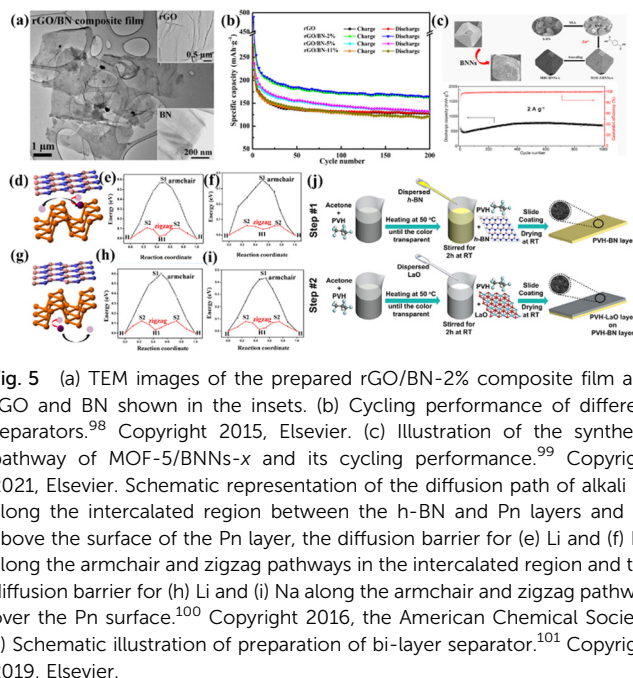
Fig. 5 (a) TEM images of the prepared rGO/BN-2% composite film and rGO and BN shown in the insets. (b) Cycling performance of different separators.[98] Copyright 2015, Elsevier. (c) Illustration of the synthesis pathway of MOF-5/BNNs-x and its cycling performance.[99] Copyright 2021, Elsevier. Schematic representation of the diffusion path of alkali (d) along the intercalated region between the h-BN and Pn layers and (g) above the surface of the Pn layer, the diffusion barrier for (e) Li and (f) Na along the armchair and zigzag pathways in the intercalated region and the diffusion barrier for (h) Li and (i) Na along the armchair and zigzag pathway over the Pn surface.[100] Copyright 2016, the American Chemical Society. (j) Schematic illustration of preparation of bi-layer separator.[101] Copyright 2019, Elsevier.

the electrolyte penetration was accelerated and the volume expansion during lithiation and delithiation was buffered. Therefore, the prepared rGO/BN binder-free film with 2 wt% BN content exhibited high reversible capacity, high rate capability, and high capacity retention during the first 200 cycles, achieving a capacity of 278 mA h g^{-1} at 100 mA g^{-1} as the anode in LIBs (Fig. 5(b)). Due to the 2D structure of BN nanosheets, porous carbon could be embedded in them using MOF-5 as a carbon precursor.[99] The prepared composites demonstrated good cycling stability and high specific capacity characteristics. The improved electrochemical performance was attributed to the high specific surface area of 1790 m^2 g^{-1} and enhanced ionic transport, resulting from the introduction of BN nanosheets.

As an important member of the alkali metal ion battery family, SIBs have become a strong competitor to LIBs due to the richer availability of sodium resources in nature and moderate energy density and power density of sodium. Datta et al.[100] demonstrated through density functional theory (DFT) calculations that the adsorption energy of Li/Na in the hetero-structures of h-BN and black phosphorus is significantly higher than the cohesive energy of the metals. This ensures that alkali metal aggregation is avoided within the anode material, leading to enhanced cycling stability. Additionally, the atomic incorporation of Li/Na resulted in an upward shift in the Fermi level in the hetero-structures, facilitating the transition from a semiconductor to a metal, and subsequently improving the conductivity. Regarding blue phosphorene, which has similar properties to black phosphorene (Fig. 5(d)–(i)), Tian et al.[102] demonstrated via calculations that when it forms a hetero-structure with h-BN, it can achieve a high theoretical capacity of 801 and 504 mA h g^{-1} for LIBs and SIBs, respectively.

Through DFT calculation, Ahuja et al.[103] demonstrated that introducing vacancy defects in the h-BN monolayer can

effectively reduce its bandgap width. When Li$^+$, Na$^+$, or K$^+$ is adsorbed, the bandgap width disappears, displaying metallic properties. The maximum theoretical capacity of alkali metal ions adsorbed on the h-BN monolayer reached 762, 572, and 127 mA h g^{-1} for Li, Na, and K, respectively; however, these materials can hardly be used as anode materials due to their poor electronic conductivity.

3.1.1.2 Separator additives. As one of the most critical components of LIBs, the separator does not directly participate in the electrochemical reaction inside the battery. However, it can prevent contact between the electrodes to avoid internal short circuits, store the liquid electrolyte, and ensure efficient ion transport during charging and discharging. However, the commonly used polymer separators in LIBs, such as polyethylene (PE) and polypropylene (PP), have poor thermal stability at high temperatures. In this case, considering the excellent thermal stability and non-conductive nature of 2D h-BN nanosheets, they are very promising to address the poor thermal stability of traditional polymer separators. He et al.[104] fabricated a bilayer separator by incorporating BN and LaO into a poly(vinylidene fluoride-hexafluoropropylene) (PVH) matrix through roll-pressing (Fig. 5(j)). The incorporation of h-BN resulted in a strong interfacial interaction with the PVH matrix, greatly enhancing the mechanical strength and thermal stability of the separator. Consequently, the bilayer separator with a thickness of 25 μm only shrank by 5.2% after annealing at 150 °C for 1 h, whereas the shrinkage rate of the commercial Celgard 2325 separator was as high as 40%. Furthermore, in another study by this team,[101] it was demonstrated that h-BN has strong adsorption energy and a large interaction area with polymers, which can prevent the delamination of bilayer organic separators and lead to an improved overall performance.

3.1.2 Alkali-metal batteries

3.1.2.1 Additives for metal surface modification. LMBs are very promising in the future based on their high energy density. However, the uncontrollable growth of lithium dendrites and volume expansion during lithium plating/stripping processes hinder their application. In this case, the high mechanical strength and thermal stability of h-BN are considered capable of restricting lithium dendrite growth, and therefore it has been widely used for the modification of lithium metal anodes. Zhu et al.[105] in situ exfoliated bulk BN into BN nanosheets using lignosulfonate (SL) and prepared a layered porous SL/BN three-dimensional composite substrate via the freeze-casting method. The exfoliated BN nanosheets effectively regulated the temperature distribution and induced uniform lithium deposition. The generation of lithium dendrites was effectively suppressed during the lithium plating/stripping process, achieving stable cycling for 500 h at 4 mA cm^{-2}. Li et al.[106] improved the performance of an LMB by introducing h-BN in Li–Zn alloy. They proposed that the uniformly distributed h-BN in the anode led to strong electrokinetic effects due to its high zeta potential, resulting in the fast transport of Li-ions. Furthermore, h-BN was found to be able to change the interface between lithium metal and solid-state electrolytes. For instance, Huang et al.[107]
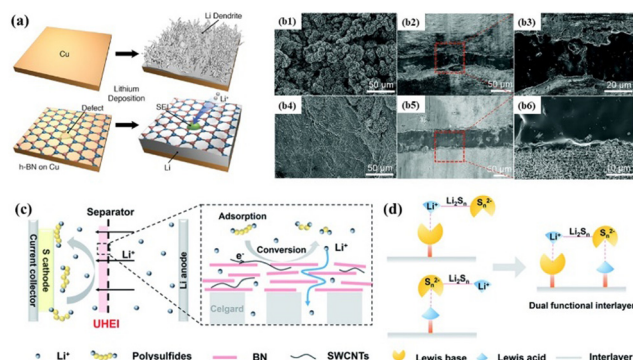
Fig. 6 (a) Schematic diagram of lithium deposition and characterizations of h-BN film.[109] Copyright 2014, the American Chemical Society. (b1) Surface SEM image of the Li electrode from the Li/PEO/Li cell. (b2) and (b3) Cross-sectional SEM images of the Li/PEO/Li cell. (b4) Surface SEM image of the Li electrode from the Li/BNNS-coated PEO/Li cell. (b5) and (b6) Cross-sectional SEM images of the Li/BNNS-coated PEO/Li cell.[112] Copyright 2019, The Royal Society of Chemistry. Schematic showing (c) Li−S battery with UHEI and (d) advantages of h-BN.[113] Copyright 2022, The Royal Society of Chemistry.

constructed an Li-BN nanosheet composite anode by adding only 5 wt% of BN nanosheets to lithium metal, triggering the transition from point contact to complete adhesion between the Li metal and ceramic solid-state electrolytes, greatly reducing the interface resistance between the electrode and the electrolyte, and thereby improving the electrochemical performance.

3.1.2.2 Building block of artificial SEI layer. Due to the high chemical reactivity of lithium metal, it easily reacts with the electrolyte to form an SEI layer. Subsequently, during cycling, uneven lithium deposition can lead to the growth of lithium dendrites and volume expansion, resulting in the rupture of the original SEI layer. This causes the growing lithium dendrites to contact the electrolyte again, forming a new SEI, which then fractures and regenerates in the following cycles. This further promotes the growth of lithium dendrites and consumption of the electrolyte, significantly reducing the Coulombic efficiency of LMBs. Previous studies have shown that the adsorption energies of Li atoms on the (001) and (110) planes of lithium metal surfaces are −1.68 and −1.85 eV, respectively, which are much greater than their adsorption energy on the h-BN surface (−0.56 eV).[108] According to calculation, h-BN can effectively block electron transfer to the electrolyte. Therefore, lithium will hardly be deposited on the surface of h-BN. Also, the introduction of h-BN can lower the migration barriers. The low lithium migration energy barrier and high stiffness of the h-BN film can synergistically promote the uniform distribution of lithium underneath the h-BN film, induce a hierarchical growth mechanism of the hidden lithium metal layer, and suppress the growth of lithium dendrites.

As the building block of an artificial SEI, this boron nitride material can be used alone or in combination with other materials. Cui *et al.*[109] deposited a layer of h-BN film on the surface of copper foil *via* chemical vapor deposition (CVD) and slurry coating. It was found that both methods could reduce the

deposition energy barrier due to the excellent chemical stability, mechanical strength, and flexibility of h-BN, as shown in Fig. 6a. Tian *et al.*[110] used pulsed laser deposition (PLD) to construct a 3D hairball-shaped h-BN structure consisting of nanosheets on the lithium metal anode, in which the stable and highly mechanically resistant h-BN coating served as an interfacial layer. Due to the flexibility of the h-BN coating and its ability to effectively alleviate the decomposition of the electrolyte, the growth of lithium dendrites during cycling was suppressed, leading to a significant improvement in cycle stability. In addition, Li *et al.*[111] proposed an integrated comprehensive strategy to construct a highly dispersed BN nanosheet and lithiophilic inorganic component (Li_2O and Li_2CO_3)-decorated 3D-graphene framework. Due to the Lewis acidity and non-conductive nature of BN in the special architecture, lithium metal could be uniformly deposited from the top to bottom. They proposed that BN and a large number of inorganic nanoparticles not only generated a uniform electric field to facilitate the migration of Li^+, but also contributed to the construction of a strong inorganic-rich SEI with high mechanical and chemical stability.

3.1.2.3 Additives in separator. The greatest safety hazard faced by LMBs is the growth of lithium dendrites, which can penetrate the separator and cause internal short circuits and heating, leading to battery combustion or even explosion. Therefore, it is particularly important to improve the separator. Hu *et al.*[114] improved the thermal conductivity of a commercial separator (Celgard 2325) by directly coating it with BN nanosheets. During cycling, the heat distribution was more uniform, resulting in more uniform lithium plating/stripping and a better Coulombic efficiency and cycling performance. Subsequently, their team integrated BN nanosheets into poly(vinylidene fluoride-*co*-hexafluoropropylene) (PVDF-HFP) using 3D printing technology.[115] The dispersed BN nanosheets not only facilitated more uniform heat distribution, but their excellent thermal stability allowed the separator to shrink by only 6% after 0.5 h of treatment at 150 °C. Zhou *et al.*[116] reported a simple synthetic strategy for large-scale fabrication by coating h-BN/polyimide (PI) on commercial polypropylene (PP) separators. Due to the presence of h-BN, the separator exhibited good wettability, thermal stability, and thermal conductivity. In addition, calculations showed that h-BN has weak adsorption on the inorganic SEI components, which can induce the formation of a more stable SEI layer, making it both capable of inhibiting lithium dendrites and dendrite blocking.

3.1.2.4 Additives in liquid electrolyte and gel-polymer electrolyte. BN nanosheets can be used as additives in both liquid electrolytes and polymer electrolytes. Huang *et al.*[117] reported the use of BN nanosheets as an additive in liquid electrolytes. The BN nanosheets could automatically and continuously flatten the lithium deposition, preventing the formation of lithium dendrites and reducing the volume changes during the lithium plating/stripping process. The B atoms on the BN nanosheets, serving as Lewis acid sites, could interact with the

Lewis basic anions in the electrolyte, lowering the concentration gradient of Li^+ ions and promoting the uniform deposition of lithium.

In gel polymer electrolytes (GPE), h-BN can play an important role. Lee et al.[118] found that lithium dendrite formation can be suppressed in the gel polymer electrolyte (GPE) by incorporating fully fluorinated polyether (PFPE)-functionalized 2D h-BN nanosheets (FBN). Even at a low FBN content of 0.5 wt%, the ion conductivity, Li^+ transference number, and mechanical modulus of GPE were significantly improved. Using a similar strategy, Reza et al.[119] embedded highly aligned BN nanosheets into a polyvinylidene fluoride composite electrolyte using the direct ink writing (DIW) method. The addition of BN nanosheets resulted in a composite electrolyte with enhanced mechanical strength, electrochemical stability, thermal safety, and a 400% increase in thermal conductivity. Moreover, studies have shown that the binding energy between $TFSI^-$ and BN/PVDF is stronger than that between Li^+ and BN/PVDF, which promotes the dissociation of LiTFSI and increases the free migration of Li^+.[120] These reports disclose that BN nanosheets can significantly improve the ionic conductivity, Li^+ transference number, mechanical modulus, tensile strength, and dendrite suppression ability of the composite polymer electrolyte.

The introduction of BN nanosheets is also beneficial in polyethylene oxide (PEO)-based electrolytes. In general, the poor mechanical properties and low ionic conductivity of PEO impede the suppression of lithium dendrite growth. Yao et al.[112] prepared a sandwich-structured BN nanosheet-coated PEO polymer electrolyte in which BN serves as a protective layer. The ionic conductivity and mechanical strength of the BN-modified PEO were significantly enhanced. Moreover, the BNNS-coated PEO polymer electrolyte strongly suppressed lithium dendrite growth (Fig. 6(b1)–(b6)). Min et al.[121] dispersed BN nanosheets (BNNSs) surface modified with SiO_2 in a PEO-based electrolyte to prepare PLSB CPE with improved thermal stability and ionic conductivity. Ding et al.[122] also demonstrated that the binding energy of $TFSI^-$ anions to unmodified h-BN was higher than that of Li^+. Therefore, the addition of h-BN can inhibit the diffusion of anions in the composite polymer electrolyte, reducing the concentration gradients and polarization, which can improve the stability of lithium deposition. There are similar reports on the positive role of h-BN nanosheets in suppressing the growth of lithium dendrite in PEO electrolytes.[123,124]

3.1.2.5 Additives in solid-state electrolytes. As additives in solid-state electrolytes (SSEs), the introduction of h-BN nanosheets can improve the ionic conductivity of SSEs, reduce the thermal runaway of batteries, and suppress the formation of lithium dendrites. To date, one of the constraints limiting the practical usage of SSEs is their relatively low ionic conductivity. In this case, it has been disclosed that the introduction of h-BN can improve the ionic conductivity of SSEs. Choy et al.[125] discovered that the addition of only 1 wt% nitride-BN to garnet-type $Li_{6.25}Al_{0.25}La_3Zr_2O_{12}$ (LALZO) SSEs increased the conductivity of the electrolyte by 30 times and the surface hardness by 6.6 times

and reduced the modulus by 6.3 times. Yang et al.[126] found the reduction of LATP SSEs by lithium metal could be suppressed effectively by using a CVD-deposited BN nano-coating on the surface of LATP. It was proposed that the defects in BN can allow lithium ions to pass through, promoting Li^+ migration and reducing the interface impedance. For example, Xia et al.[127] constructed a three-dimensional organic/inorganic composite coating by spraying BN-based release agents (BNRA) on the surface of LATP. The BNRA layer not only protected LATP but also formed Li–N bonds *in situ*, facilitating the migration of Li ions through the BN defects at the BNBR/Li interface. Furthermore, the BNRA layer eliminated the risk of thermal runaway by rapid in-plane diffusion.

It is worth mentioning that hybrid solid electrolytes (HSE) have been widely studied for use in all-solid-state lithium-based batteries due to their high ionic conductivity, mechanical strength, enhanced electrochemical stability, and effective suppression of lithium dendrite growth. Park et al.[128] prepared a standalone hybrid solid electrolyte film using poly(vinylidene fluoride-*co*-hexafluoropropylene) (PVDF-HFP) as the matrix and $Li_{6.28}Al_{0.24}La_3Zr_2O_{12}$ (LALZO)/h-BN composite ceramic fillers as the filler. The optimal proportion of h-BN (10 wt%) in the HSE film reduced the crystallinity of the PVDF-HFP matrix, increased the proportion of electroactive β-phase, and improved the mechanical strength of the HSE film, as well as effectively suppressed lithium dendrite growth.

3.1.3 Alkali–S/O batteries

3.1.3.1 The host material of sulfur. Although the lithium metal anode discussed earlier has great potential, its energy density is still limited by the cathode material when matched with the currently used commercial metal oxide positive electrodes. However, the development of L–S batteries has been hindered by issues including the shuttle effect of lithium polysulfides (LiPSs) during charge and discharge, poor electronic conductivity of sulfur cathodes, and large volume changes. Therefore, the key scientific problem currently faced by Li–S batteries is to find effective nano-anchoring materials to immobilize soluble LiPSs and suppress their shuttle effect. Through DFT calculations, Jin et al.[129] proposed that doped and defective BN nanosheets can serve as chemical fixatives for soluble LiPS species. Dai et al.[130] found that the nitrogen vacancies in BN play a critical role in the conversion and fixation of LiPSs and can enhance the diffusion of lithium ions in the cathode. It is noteworthy that BN nanosheets have been frequently used in combination with materials with high conductivity (MXene,[131] graphene,[132–134] graphene oxide,[133,135] carbon nanotubes,[136,137] etc.) to ensure fast electron transfer.

3.1.3.2 Separator in Li–S batteries. Many reports proved that the modification of the separator is an effective and straightforward strategy to alleviate the shuttle effect and enhance the electrochemical performance of Li–S batteries.[138] Thus, considering the 2D structure and excellent mechanical properties of BN nanosheets, they can be designed to modify the separator. Ungyu et al.[139] designed a multifunctional three-layered separator consisting of carbon layers and h-BN layers, which effectively suppressed the shuttle effect of polysulfides.

In addition, it effectively protected the lithium metal in the anode from the influence of polysulfides during cycling, enabling stable operation of the anode and exhibiting good cycling retention performance. Using a simple BN nanosheet coating, Chen et al.[140] prepared a multiple-layer separator by coating a thin layer of functional BN (FBN) nanosheets on a commercial Celgard separator. Due to the strong electrostatic interaction between the negatively charged polysulfide products and FBN nanosheets, this BN-modified separator could limit the migration of dissolved PSs through the separator, enhance Li^+ migration, suppress the internal shuttle effect, and enable the cell to achieve a high capacity, high-rate capability, and long-term cycling stability. Similarly, Xiong et al.[141] prepared a separator composed of P-doped BN and graphene oxide, which provided a synergistic effect of a physical barrier and chemical adsorption for dissolved polysulfides, showing alleviated polarization and promoted kinetics in the cell. Chen et al.[142] reported that the introduction of BN in a CoB and rGO-modified PP separator could effectively restrict the diffusion of polysulfides through enhanced chemical adsorption with LiS_nLi^+–N bonding.

Li et al.[113] reported the preparation of an ultra-thin and highly efficient BN/single-walled carbon nanotube (BN/SWCNT) interlayer (UHEI), which not only hindered the diffusion of polysulfides but also promoted further redox reactions to facilitate the transport of Li^+. Additionally, UHEI could significantly improve the electrochemical performance of Li–S batteries at a high-sulfur (10 mg cm^{-2}) and low electrolyte/sulfur (E/S ratio of 8 μL mg^{-1}) loading, as manifested by the higher plateau capacities and lower polarization during discharge.

BN nanosheets can increase mechanical strength greatly. For example, a BN-modified PVDF separator could enhance the compressibility of batteries, which could maintain stable cycling 20 times even when subjected to a pressure of 20 MPa.

3.1.3.3 Solid-state electrolytes additives. The use of SSEs is considered an effective approach to simultaneously address the shuttle effect and suppress lithium dendrite growth. The introduction of BN nanosheets in SSEs can improve the interface compatibility between the electrode and electrolyte. Ci et al.[143] prepared a fully solid-state electrolyte, $Li_7P_3S_{11}$, with a small amount of BN nanosheets, in which the BN nanosheets could partially isolate the $Li_7P_3S_{11}$ solid electrolyte and metallic lithium, thereby improving the interface compatibility between the electrode and electrolyte The solid-state Li–S cells using BN-combined $Li_7P_3S_{11}$ as the solid electrolyte exhibited good cycling stability and high Coulombic efficiency.

In the case of polymeric-based solid-state electrolytes, BN nanosheet additives can not only enhance their mechanical strength but also improve their ionic conductivity. Zheng et al.[144] developed a BN nanosheet-doped polymeric electrolyte (BN-PEO-PVDF) for solid-state lithium batteries. In addition, BN nanosheet additives can promote the thermal response of polymeric electrolytes, leading to faster thermal equilibration and more uniform ion transport in the BN-PEO-PVDF electrolyte.

3.2 Application of g-C_3N_4 in alkali metal-based batteries and alkali metal ion batteries

3.2.1 Alkali metal ion batteries

3.2.1.1 Electrode material additives. Graphitic carbon nitride (g-C_3N_4), an organic polymer with a graphene-like structure, has been extensively studied in photocatalysis due to its small band gap, large specific surface area, good chemical stability, low toxicity, and high yield. On one hand, the feasibility of pure g-C_3N_4 as an anode materials in LIBs was also studied through DFT calculation. M. Hankel et al.[145] found that when lithium intercalates into the triangular pores of g-C_3N_4, its adsorption energy (E_{ad}) is as high as −4.2 eV, exceeding the desorption energy of the bulk Li (−3 eV), which makes the adsorbed Li atom difficult to desorb from the structure, resulting in an unstable structure, poor conductivity, and limited reversible capacity. In this case, the introduction of defects in g-C_3N_4 can improve its electrochemical performance in LIBs[146] to a certain degree. However, g-C_3N_4 showed a poor electrochemical performance as the anode in LIBs in most cases.

On the other hand, the combination of g-C_3N_4 with electrode materials can improve their electrochemical performance because of its N-rich content and 2D structure. It was later discovered that due to the presence of nitrogen, g-C_3N_4 can form hydrogen bonds with anode materials (such as MoS_2, SnS_2, $Li_4Ti_5O_{12}$, SnO_2, Sn, and GO)[147–156] in LIBs, forming a single hybrid material that utilizes the 2D–2D molecular interactions between them.

Shao et al.[157] synthesized $NiCo_2O_4$ directly grown on porous g-C_3N_4 nanosheets, where the interconnected $NiCo_2O_4$ nanoparticles were embedded into the porous nanosheets. Complete coverage of the g-C_3N_4 nanosheets minimized the formation of SEI layers, leading to a significant synergistic enhancement in both electrochemical activity and stability of the hybrid material. Similarly, Su et al.[158] chose to grow ordered CuO nanorods on 2D Cu/gC_3N_4 nanosheets, creating a graded CuO@Cu/g-C_3N_4 nanorod film. The resulting film exhibited exceptional stability and cycling performance in both CuO and CuO-based nanoscale architectures, delivering a discharge-specific capacity of 726 mA h g^{-1} after 200 cycles at 0.1C and 457 mA h g^{-1} after 625 cycles at 1C. The presence of porous g-C_3N_4 endowed the prepared structure with more active sites, facilitating Li^+ transport and volume change accommodation. Yao et al.[159] synthesized an MoO_3MoO_2 heterojunction anchored on two-dimensional g-C_3N_4 nanosheets by calcining ammonium molybdate with urea. The two-dimensional porous structure of g-C_3N_4 provided abundant active sites for Li-ion storage, enhanced the conductivity, and mitigated the volumetric expansion effect during the charge–discharge cycle. In addition, it has been reported that g-C_3N_4 can buffer the volume change in anode materials. Lin et al.[160] reported the synthesis of a layer-structured g-C_3N_4@WS_2 composite material *via* the solvothermal reaction. The synthesized g-C_3N_4@WS_2 composite material provided abundant reactive sites for lithium storage and sufficient voids to buffer the volume changes of WS_2 nanoparticles.

Furthermore, the rich N content in g-C_3N_4 can provide more active sites to store lithium. Sun et al.[161] synthesized a laminated

g-C$_3$N$_4$@rGO composite material (g-C$_3$N$_4$@rGO), (Fig. 6(a)), which exhibited excellent cyclic stability (899.3 mA h g^{-1} after 350 cycles at 500 mA g^{-1}) and a significant rate performance (595.1 mA h g^{-1} after 1000 cycles at 1000 mA g^{-1}). The presence of g-C$_3$N$_4$ in the synthesized g-C$_3$N$_4$@rGO composite material increased the interlayer spacing of rGO and provided rich *n*-active sites and microporous structure, thereby greatly improving the Li storage performance. Wen *et al.*[162] achieved a significant improvement in performance by uniformly dispersing red phosphorus nanoparticles between the layers of rGO-C$_3$N$_4$ through a simple high-energy ball milling process. This was attributed to the interface connection formed by P–N and P–C bonding between the red phosphorus and rGO-C$_3$N$_4$ skeleton, which created a smooth Li$^+$/e$^-$ diffusion channel and enhanced its mechanical properties. Cui *et al.*[163] found that the incorporation of g-C$_3$N$_4$ nanosheets into a CuCo$_2$O$_4$ nanowire array could not only shorten the diffusion distance of Li$^+$ and the electron transfer pathway but also provide more active sites for Li$^+$ diffusion to the electrolyte, which could buffer the volume expansion and aggregation of CuCo$_2$O$_4$. Sun *et al.*[164] found that g-C$_3$N$_4$ can have a similar effect on Co$_{1-x}$S anode materials in LIBs. Kim *et al.*[165] synthesized honeycomb-like Se-doped g-C$_3$N$_4$ (Se-H-g-C$_3$N$_4$) *via* pyrolysis and selenization, where selenium served as a stronger electron-accepting unit than carbon and nitrogen. Selenium doping also had a significant impact on the electronic structure of the carbon skeleton. This is because Se atoms significantly enlarged the gap between the carbon layers, creating more active sites for lithium-ion storage and accelerating the diffusion rate.

Moreover, g-C$_3$N$_4$ can act as a protective layer on the surface of anode materials. For example, Pan *et al.*[166] synthesized a graphene-like carbon nitride/Mo$_2$CT$_x$ (g-C$_3$N$_4$/Mo$_2$CT$_x$) hybrid material *via* the *in situ* conversion of urea to g-C$_3$N$_4$ and achieved the exfoliation of Mo$_2$CT$_x$ MXene with the construction of a protective layer. Compared to pure Mo$_2$CT$_x$ (19.2% and 101.4 mA h g^{-1}), g-C$_3$N$_4$/Mo$_2$CT$_x$ exhibited a significantly improved initial Coulombic efficiency (70.8%) and lithium storage performance (525.8 mA h g^{-1}), respectively (Fig. 7(b)).

In SIBs, the incorporation of g-C$_3$N$_4$ in carbon can enhance the electrochemical performance of SIBs. Taylor *et al.*[167] obtained stacked multilayered C/g-C$_3$N$_4$ composites by heating a mixture of inexpensive urea and asphalt in a single pot, which exhibited twice the sodium storage capacity (254 mA h g^{-1}) of the pristine g-C$_3$N$_4$ composite (Fig. 7(c)). Similar phenomena were also observed in carbon/g-C$_3$N$_4$ composites. The high crystallinity of C$_3$N$_4$, its 2D nanosheet structure with abundant edges and pores as well as the high concentration of pyridinic N contribute to important factors in enhancing sodium storage[168] (Fig. 7(d1)–(d6)). Similarly, in the study by Wu *et al.*,[169] a defective g-C$_3$N$_4$/graphene heterojunction was prepared by ball milling, and the nitrogen-containing functional groups were controlled to improve the sodium storage capacity.

It has also been proven that the combination of g-C$_3$N$_4$ and conversion-type anode materials can enhance the electrochemical performance. Avesh *et al.*[152] reported that g-C$_3$N$_4$ in the ZnS/g-C$_3$N$_4$ composite could prevent the agglomeration of nanoparticles during the charge/discharge process. The presence
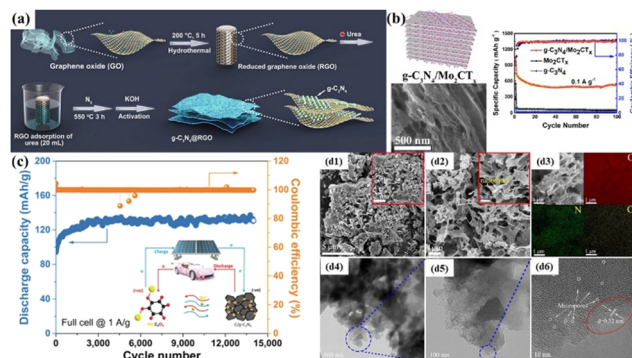

Fig. 7 (a) Procedure for the synthesis of g-C$_3$N$_4$@RGO.[161] Copyright 2018, the American Chemical Society. (b) Illustration and SEM images of the prepared g-C$_3$N$_4$/Mo$_2$CT structure, together with the cycling stability of the assembled battery at a current density of 0.1 A g^{-1}.[166] Copyright 2021, Elsevier. (c) Configuration of a C/g-C$_3$N$_4$ Na full cell consisting of a positive electrode of Na$_2$C$_6$O$_6$ and a negative electrode of C/g-C$_3$N$_4$ and cycling performance of a C/g-C$_3$N$_4$ Na full cell at 1 A g^{-1}.[167] Copyright 2019, Wiley-VCH. SEM images of (d1) PTI and (d2) MSGM together with high-magnification images in the inset, respectively. (d3) EDS elemental mappings and (d4)–(d6) TEM images of MSGM.[168] Copyright 2021, Elsevier.

of g-C$_3$N$_4$ alleviated the harmful volume change effect of Li$^+$/Na$^+$ ions during their shuttle in ZnS, leading to the composite anode exhibiting a high reversible capacity and initial Coulombic efficiency. Similarly, Im *et al.*[170] found that the presence of g-C$_3$N$_4$ could restrain the severe strain caused by volume changes during the sodium storage in SnS$_2$.

Furthermore, the presence of g-C$_3$N$_4$ can enhance the K storage in carbon materials due to its large surface area and abundant active sites. For example, Zhang *et al.*[171] designed and synthesized a one-dimensional/two-dimensional C$_3$N$_4$/rGO composite material as a host for potassium ions. The resulting composite exhibited a significant specific capacity of 464.9 mA h g^{-1} after 200 cycles at 1 A g^{-1} and 228.6 mA h g^{-1} after 1000 cycles at 10 A g^{-1}.

3.2.2 Alkali–metal batteries

3.2.2.1 Anode substrate and protective layer. The natural formation of a ring-shaped micro-electric field induced by the six p-electrons of N atoms in the tri-*s*-triazine units of g-C$_3$N$_4$ not only endows g-C$_3$N$_4$ with better lithiophilicity, leading to the formation of more Li nucleation sites, but also significantly reduces the Li nucleation overpotential. This suggests that g-C$_3$N$_4$ holds great potential as a promising material for application in LMBs.[172,173] Due to its lithiophilic and insulation properties, g-C$_3$N$_4$ can be combined with other conductive materials as both a lithium metal anode substrate and a lithium metal negative electrode protective layer. Yang *et al.*[174] coated g-C$_3$N$_4$ on the surface of nickel foam to combine the lithiophilicity of g-C$_3$N$_4$ with the 3D structure of nickel foam, thereby inhibiting lithium dendrite growth and reducing the volume expansion during the deposition and stripping of lithium metal (Fig. 8(a)). Hence, the lithium metal anode based on g-C$_3$N$_4$@Ni foam displayed remarkable electrochemical performances, including high Coulombic efficiency (maintaining 98% after 300 cycles),
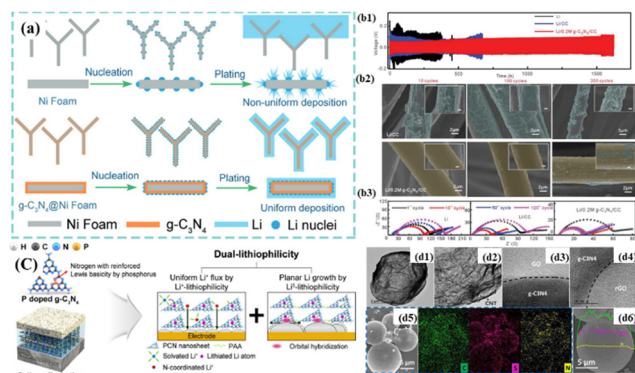
Fig. 8 (a) Schematic of the Li nucleation and plating process on Ni foam and g-C$_3$N$_4$@Ni foam.[174] Copyright 2019, Wiley-VCH. (b1) Voltage profiles of Li–Li symmetric batteries with bare Li, Li/CC, and Li/0.2 mg-C$_3$N$_4$/CC electrode at a current density of 2.0 mA cm^{-2}. (b2) SEM images of Li/CC and Li/0.2 mg-C$_3$N$_4$/CC after 10, 50, and 100 cycles in Li–Li symmetric batteries. (b3) Nyquist plot of impedance spectra of Li–Li symmetric batteries with Li/CC and Li/0.2 mg-C$_3$N$_4$/CC electrode after different cycles.[176] Copyright 2019, Wiley-VCH. (c) Schematic illustration of the lithium deposition mechanism under dual-lithiophilic interfacial layer.[177] Copyright 2022, Elsevier. (d1) and (d2) High-resolution TEM (HRTEM) images of GO/g-C$_3$N$_4$/CNT (d3) and rGO/g-C$_3$N$_4$/CNT (d4). (d5) SEM image and EDS elemental mapping of rGO/g-C$_3$N$_4$/CNT/S. (d6) Elemental line scan of rGO/g-C$_3$N$_4$/CNT/S.[178] Copyright 2019, the American Chemical Society.

the ultra-long lifespan of 900 h, and low overpotential during Li deposition of 1.0 mA h cm^{-2} (<15 mV). Similarly, the g-C$_3$N$_4$-rGO composite with high elasticity and wrinkled structure as a lithium metal anode substrate showed a lower nucleation overpotential and small volume expansion during cycling.[175]

3.2.2.2 Components in artificial SEI layer. Some studies showed that g-C$_3$N$_4$ can be a good candidate material as a component of the artificial SEI layer because of its rich N-containing functional groups and non-conducting nature. Tu et al.[179] prepared a g-C$_3$N$_4$ artificial SEI layer with a thickness of only 1 nm on lithium foil. The abundant and uniformly distributed N species in g-C$_3$N$_4$ could form transient Li–N bonds with lithium ions, thereby regulating the flux of lithium ions and enabling stable plating/stripping processes. Kang et al.[176] designed a uniform and dense artificial interface by wrapping carbon nanofibers in commercial carbon cloth using a g-C$_3$N$_4$ coating. Lithium metal could selectively deposit in the interlayer between g-C$_3$N$_4$ and CC, where g-C$_3$N$_4$ as an artificial interphase exhibited favorable lithiophilic properties and was capable of regulating the distribution of Li ions and eliminating dendritic hotspots. Thus, uniform lithium deposition could be achieved for this substrate, leading to large-capacity metal Li storage (Fig. 8(b1)–(b3)). Furthermore, it is beneficial to coat g-C$_3$N$_4$ on the surface of MXenes[180] and LiMg–LiH[181] as an artificial SEI to improve the performance of LMBs.

It is also effective to coat g-C$_3$N$_4$ on lithium metal to enhance the electrochemical performance of LMBs.[182]

3.2.2.3 Separator additives. Differing from previous reports on artificial protective layers, Kim et al.[177] constructed a dual

lithiophilic interlayer on the surface of the separator, which although coated onto the separator, effectively functioned similarly to an artificial SEI layer due to its direct contact with the lithium metal. The constructed dual lithiophilic interlayer exhibited affinity for both Li$^+$ and Li^0, featuring enhanced Lewis basicity and orbital hybridization concepts. Furthermore, the strong interaction between Li$^+$ and the dual lithiophilic interlayer facilitated the charge transfer process. Under the driving force of orbital hybridization, the deposition of a lithium metal layer beneath the dual lithiophilic interlayer occurred in a planar growth mode, alleviating the decomposition of the electrolyte (Fig. 8(c)). The Li/Li symmetric cells employing the dual lithiophilic interlayer functioned for over 400 cycles at 2 mA cm^{-2} and 2 mA h cm^{-2}.

3.2.2.4 Additives in electrolyte and gel-polymer electrolyte. As an additive in polymer electrolytes, g-C$_3$N$_4$ can play a unique role in improving their electrochemical performance. Li et al.[183] utilized g-C$_3$N$_4$ as an additive to mix with [bis(trifluoro-methanesulfonimide)lithium salt/di(ethylene glycol)dimethyl ether] (LiTFSI-DGM), creating a slurry-like polymeric electrolyte. Benefiting from the advantages of high mechanical strength and layered structure availability, g-C$_3$N$_4$ effectively inhibited the growth of lithium dendrites. This slurry-like electrolyte exhibited a reduced anode-electrolyte interface resistance (115 Ω cm^2) and decreased Li plating/stripping overpotentials (reaching as low as 50 mV and 100 mV at 0.5 mA cm^{-2} and 2 mA cm^{-2}, respectively). Zhang et al.[184] introduced g-C$_3$N$_4$ nanosheets in a PVdF-HFP based solid polymer electrolyte (SPE). This effectively disrupted the ordered arrangement of the polymer segments in the solid-phase electrolyte, reducing the crystallinity of the solid electrolyte and facilitating the faster migration of lithium ions within the PVDF-HFP matrix. Moreover, the pyridinic N on g-C$_3$N$_4$ nanosheets can be considered as a Lewis base, promoting the dissociation of LiTFSI and increasing the concentration of free lithium ions. In addition, the presence of 2D g-C$_3$N$_4$ can improve the mechanical strength, reduce the crystallinity, suppress the formation of lithium dendrites,[185] and enhance the thermal stability in PVDF-HFP based electrolytes.[186]

The addition of g-C$_3$N$_4$ in the PEO electrolyte can significantly enhance its cycling stability towards lithium anodes given that g-C$_3$N$_4$ widens the electrochemical window of the electrolyte, preventing direct contact between PEO and lithium.[187] The presence of electronegative N species in g-C$_3$N$_4$ ensures the uniform deposition of lithium ions. Because g-C$_3$N$_4$ has abundant Lewis basic active sites, the addition of g-C$_3$N$_4$ in PEO-based electrolytes can regulate the distribution of Li$^+$ ions, thereby inhibiting the growth of lithium dendrites.[188] Symmetrical cells assembled with this CSE successfully cycled for 1400 h at 0.1 mA cm^{-2} and 60 °C. Additionally, PCN reduced the crystallinity of PEO and promoted the dissociation of LiTFSI, effectively enhancing the Li$^+$ conductivity of the electrolyte (3.47×10^{-4} S cm^{-1} at 60 °C).

Besides the enhancement in mechanical strength and thermal stability, the presence of uniformly distributed g-C$_3$N$_4$ nano-fillers can significantly reduce the crystallinity of the

polymer electrolyte and promote the dissociation of Na^+ through the interaction between surface N atoms and sodium salts, resulting in a better performance.

3.2.2.5 Solid-state electrolyte additives. The addition of g-C_3N_4 nanosheets to solid-state electrolytes can change the contact between the lithium metal and SSEs. Huang et al.[189] demonstrated that the addition of g-C_3N_4 nanosheets to molten lithium could transform the point contact between the lithium metal and the garnet-type solid electrolyte into intimate contact. Additionally, the increased viscosity of the molten lithium reduced its surface tension, significantly enhancing the energy to suppress lithium dendrite growth.

As a 2D nanosheet, g-C_3N_4 can be assembled in the interlayer of inorganic solid electrolytes. Wang et al.[190] fabricated a layered inorganic solid electrolyte (LLZO/CN LISE) with a thickness of 30 μm by assembling LLZO nanosheets into a layered framework and growing g-C_3N_4 *in situ* in the interlayer spacing. At 25 °C, the LLZO/CN LISE exhibited an ion conductivity of 2.50×10^{-4} S cm^{-1}, providing a high ion conductivity of 167 mS. Moreover, g-C_3N_4 formed tight bonding with the adjacent LLZO layers, resulting in excellent mechanical properties in the LLZO/CN LISE.

3.2.3 Additives in alkali–S/O battery

3.2.3.1 As sulfur host. Because of the rich N content and high polarity of g-C_3N_4, it exhibits superior chemical adsorption capability for LiPSs, effectively suppressing their dissolution in the electrolyte. In its earliest application in 2016, Pang et al. utilized graphitic carbon nitride (C_3N_4) as an efficient sulfur-based matrix to enhance the cycling stability of lithium-batteries.[191,192] The pyridinic nitrogen-rich structure in g-C_3N_4 exhibits superior chemical adsorption capability for LiPSs. According to DFT calculations,[193] g-C_3N_4 is favorable for achieving anchoring effects toward LPSs through both chemical bonding and physical confinement of the relevant species. Also, g-C_3N_4 provides an appropriate binding energy, enhancing the redox kinetics. The dispersion interactions are mainly concentrated near the sulfur atoms, and the bonding and charge transfer between Li–N/C–S result in a strong anchoring effect. Additionally, the strong coupling interactions formed by g-C_3N_4 can alleviate the interaction between LPSs and the solvent, thereby playing a dissolution-mitigating role.

However, although feasible according to theoretical calculation, the limited conductivity of g-C_3N_4 hampers its practical application. In this case, BN-based composites can overcome this disadvantage of g-C_3N_4. Kuang et al.[194] fabricated a 3D lightweight and porous C_3N_4 nanosheet@rGO (g-C_3N_4@rGO) network as a sulfur host. PCN incorporated in the nanocomposite provided a high nitrogen content (18.99%) for chemically anchoring lithium polysulfides, while rGO in the nanocomposite facilitated rapid electron transfer. Furthermore, the high surface area of the 3D network provided open channels for ion diffusion and electrolyte accessibility. Employing a similar strategy[178,195] (Fig. 8(d1)–(d6)), rGO/g-C_3N_4/CNT was reported as a host of LiPSs. Besides the chemical adsorption of rGO and CNT, the enriched nitrogen (N) atoms in g-C_3N_4 exhibit strong chemical adhesion for anchoring LiPSs. The dual immobilization mechanism effectively alleviates the "shuttle effect" in Li–S batteries. Thus, the discharge capacity of the rGO/g-C_3N_4/CNT/S cathode after 500 cycles was 620 mA h g^{-1}, with a low capacity decay rate of only 0.03% at 1C. The elevated nitrogen content in g-C_3N_4 effectively enhances the cycling stability of Li–S batteries and their chemical interactions with polysulfides.[196]

Furthermore, due to the significantly increased number of active sites facilitated by the high specific surface area of g-C_3N_4, its combination with materials such as graphene,[197] carbon hybrid cages,[198] carbon nanotubes (CNT),[199,200] Ti_xO_y–Ti_3C_3,[201] rGO (polypyrrole-coated g-C_3N_4),[202] carbon cloth,[203] $MoSe_2$,[204] MXenes[205] and Ni[206] as an S host resulted in excellent suppression of polysulfide shuttle effects. In particular, Chen et al.[207] synthesized a composite of ultrathin MoS_2 nanosheets and nitrogen-rich g-C_3N_4. The strong chemical interactions between MoS_2 and nitrogen-rich g-C_3N_4 with lithium polysulfides effectively hindered the shuttle effect in Li–S batteries, resulting in a stable cycling performance and outstanding rate capability, while also efficiently suppressing self-discharge behavior.

In addition to composites with other materials, Huang et al.[208] utilized heterojunctions formed between two precursors of g-C_3N_4 to effectively tune its electronic cloud structure and interface adhesion energy. This close g-C_3N_4/g-C_3N_4 interface imparted significantly accelerated reaction kinetics and enhanced ion and electron transport.

3.2.3.2 Separator additives. The coating of g-C_3N_4 on the surface of the separator is also effective in trapping and fixing polysulfides. Wang et al.[209] coated commercial separator surfaces with transition metal-coordinated g-C_3N_4 and crystalline carbon (M-C_3N_4/C). This coating exhibited excellent trapping ability and rapid conversion capability for polysulfides. The uniformly distributed transition metals on g-C_3N_4/C serve as active centers to regulate the behavior of polysulfides, displaying strong chemical adsorption capacity and high catalytic activity towards polysulfide conversion. When combined with other functional materials, the capability of g-C_3N_4 to trap polysulfides can be further improved. Wang et al.[210] designed a novel dual-functional separator, where a self-assembled FeOOH layer was firmly formed on the PP separator surface to chemically capture soluble polysulfides and prevent shuttle effects. Subsequently, a coated g-C_3N_4/KB layer was introduced to greatly enhance the migration of lithium ions and physically confine the migration of the intermediate products. Consequently, the batteries employing this dual-functional separator (referred to as G-SFO) achieved remarkable rate capacities (1000, 901, and 802 mA h g^{-1} at 0.5, 1, and 2C, respectively).

The doping to g-C_3N_4 can further improve the trapping capability, as illustrated by Co-doped g-C_3N_4,[211] in which doped heteroatoms can play a role in catalytic conversion, effectively mitigating shuttle effects.

3.2.3.3 The catalysts in Li–O battery. Due to its high nitrogen content, g-C_3N_4 facilitates a simple synthesis process and

possesses more active reaction sites compared to other nitrogen-doped carbon materials, making it considered a viable non-metallic electrocatalyst for the oxygen reduction reaction (ORR). Liu et al.[212] reported the synthesis of a non-metallic, standalone mesoporous graphene@graphitic carbon nitride (g-C_3N_4) composite air cathode material. In this material, the g-C_3N_4 nanosheets functioned as an efficient electrocatalyst, while the mesoporous graphene nanosheets provided spatial accommodation for Li_2O_2 deposition and promoted the electron transfer. The results demonstrated that compared to the pure graphene air electrode, the graphene@g-C_3N_4 composite air electrode exhibited a lower charging plateau by 0.48 V, a higher discharging plateau by 0.13 V, and a discharge capacity approaching 17 300 mA h g^{-1}.

Moreover, the conductivity and catalytic activity of g-C_3N_4 can be enhanced by incorporating it in other materials that possess better conductivity. For instance, the combination of g-C_3N_4 with Co,[213] Fe,[214] and Ni–Co_3O_4[215] among others, as non-precious metal composites has been investigated as effective catalysts in fuel cells and LOBs. These composite materials exhibit excellent ORR (oxygen reduction reaction) and OER (oxygen evolution reaction) activity and durability, which are comparable to that of commercial Pt/C catalysts. Shui et al.[216] utilized a low-cost non-precious metal composite of $LaNiO_3$ and g-C_3N_4 as a dual-functional electrocatalyst for the air electrode in lithium–oxygen batteries. The compositional strategy altered the electronic structure of $LaNiO_3$ and g-C_3N_4, ensuring a higher Ni^{3+}/Ni^{2+} ratio and increased hydroxyl surface adsorption on CNL, thereby promoting the oxygen reduction reaction (ORR) and oxygen evolution reaction (OER). Yu et al.[217] synthesized a composite material of $CoFe_2O_4$/g-C_3N_4, where the layered structure of g-C_3N_4 facilitated the transport of oxygen and lithium ions and hindered the aggregation of $CoFe_2O_4$ particles. During the charge–discharge reactions, the $CoFe_2O_4$ material accelerated the decomposition of Li_2O_2, thereby reducing the electrode polarization.

In addition, single-atom metal catalysts have been demonstrated to decrease costs and more effectively utilize precious metals. Based on this, Qian et al.[218] synthesized single-atom Pt catalysts (Pt-CNHS) supported on hollow ultrathin g-C_3N_4 nanosheets through the liquid-phase reaction between g-C_3N_4 and H_2PtCl_6. The single-atom Pt catalyst exhibited high electrochemical activity. Based on the experimental results and DFT calculations, the excellent electrocatalytic activity of Pt-CNHS can be attributed to its large specific surface area, enhanced conductivity, efficient interfacial mass transfer between Pt atoms, and porous structure.

Inspired by the excellent performance of g-C_3N_4 in photocatalysis, Zhang et al.[219] designed a novel photo-responsive cathode via the in situ growth of Co-doped C_3N_4 (Co-C_3N_4) on carbon paper (CP). The Co doping not only enhanced the conductivity and electrocatalytic ability of C_3N_4 but also facilitated bandgap tuning, broadening the wavelength range of light response and enhancing the photocatalytic performance of C_3N_4. Anik et al.[220] utilized g-C_3N_4/rGO nanocomposites as photocatalysts for efficient light-assisted charging in

lithium–oxygen batteries. The formation of new C–C bonds between g-C_3N_4 and rGO during the decomposition process of melamine led to a red shift in the absorption edge of the nanocomposites. This red shift resulted in a reduction in the optical band gap of the nanocomposites, enhancing the capture and utilization of visible light. By employing the nanocomposites as photoelectrodes in lithium–oxygen batteries, a significant reduction in charging potential, particularly at high current densities, was achieved, leading to an improved cycling performance by the batteries.

3.3 Application of MMT and VMT in alkali-based batteries

3.3.1 Alkali metal ion batteries

3.3.1.1 Electrode material additives. Montmorillonite (MMT) is a naturally abundant and cost-effective clay mineral consisting of two layers of silica tetrahedra and aluminum octahedra sandwiched between them. The intercalation of hydrated cations occurs between the layers to balance the charge through van der Waals forces. MMT possesses a high surface area, cation intercalation/exchange capacity, scalability, and excellent thermal/hydrothermal stability, making it highly promising for applications such as adsorbents, catalysts, sensors, and filtration membranes.

In the field of energy storage, MMT nanosheets are not suitable to act as anode materials due to their non-conductive nature although there have been several reports on this.[221,222] However, MMT can be employed as an auxiliary material in combination with other anode materials to enhance their electrochemical behavior. Shen et al.[223] disclosed that the addition of MMT nanosheets could enhance the structural stability and reversibility of hard carbon materials, as shown in Fig. 9(a) and (b).

The incorporation of MMT facilitates the formation of a mechanically stable SEI layer, reducing the electrolyte decomposition and maintaining the integrity of the electrode
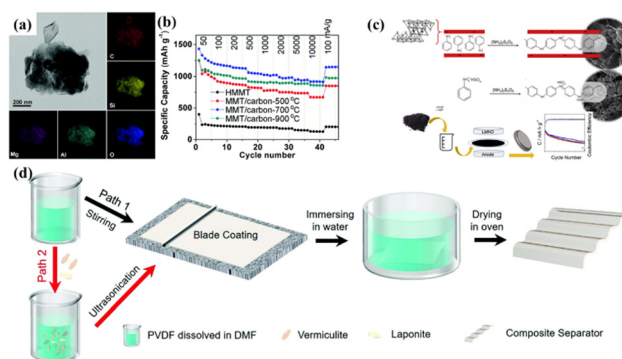
Fig. 9 (a) TEM image and element mapping of MMT/carbon-700 °C. (b) Rate performance at a range of current densities from 50 to 10 000 mA g^{-1}.[223] Copyright 2020, The Royal Society of Chemistry. (c) Polymerization of anilinium in the interlamellar space of MMT forms an intercalated nanocomposite, where the emeraldine positive charges are balanced with the negative charges of MMT.[224] Copyright 2021, Elsevier. (d) Schematic illustration of the preparation of composite separators.[225] Copyright 2022, The Royal Society of Chemistry.

structure. Yang et al.[88] utilized MMT to construct a novel electrode/electrolyte interface for lithium-graphite dual-ion batteries (DIBs). The prepared SEI film could modulate the anion intercalation/deintercalation behavior, facilitating the rapid migration of anions, while preserving the graphite structure from degradation. Also, MMT may react with the electrolyte decomposition products, such as HF, potentially avoiding the corrosion of battery components under high voltage conditions.

3.3.1.2 Separator additives

MMT as additives. Due to the high porosity and thermal stability of MMT, it has been extensively applied in the field of separators. Lanceros-Mendez et al.[226] prepared MMT/P(VDF-TrFE) porous films with varying MMT contents using a solvent-casting method for LIBs. The encapsulation of MMT increased the average pore size, porosity, and electrolyte solution absorption of the film. Also, the addition of fillers enhanced the mechanical properties of the film. The presence of clay slightly improved the ionic conductivity, while also significantly improving the temperature stability. Thus, MMT nanosheets can be an efficient additive to enhance the thermal stability, mechanical strength, and ionic conductivity of polymer-based separators due to their inorganic components and 2D structure[224,227,228] (Fig. 9(c)).

VMT as additives. Due to the high stability of sepiolite at temperatures above 1000 °C, Pol et al.[229] chose to coat one side of polypropylene with a 7 μm layer of 1:9 sepiolite to PVDF to enhance the thermal stability of the separator. Calorimetry experiments showed that the sepiolite-PVDF-modified PP had a lower heat release rate (101.7 J g^{-1} for PP and 83.16 J g^{-1} for the modified separator) and a slightly higher melting point (ΔT = +3.38 °C). This demonstrates that the sepiolite-modified separator improved the safety. Further research on increasing the amount of sepiolite will result in separators with even higher melting points. Zhang et al.[225] incorporated sepiolite nanoparticles (VMT) and LAPONITE® nanoparticles (LPT) in a polyvinylidene fluoride (PVDF) matrix to prepare organic–inorganic composite membranes for LIBs (Fig. 9(d)). The membrane exhibited the best performance when the ratio of the two inorganic nanoparticles was 1:1. The prepared separator demonstrated the highest ionic conductivity (0.72 mS cm^{-1}) and the lowest interfacial impedance (283 Ω) at room temperature. Furthermore, the addition of VMT and LPT nanoparticles effectively reduced the thermal shrinkage, improved the thermal dimensional stability, electrolyte uptake, and porosity of the membrane. Tu et al.[230] discovered that the addition of two-dimensional sepiolite nanosheets greatly improved the thermodynamic instability of PVDF/N,N-dimethylacetamide (DMAc) solution, leading to the formation of elongated finger-like porous structures. When the content of the sepiolite nanosheets (VNs) was 7.0 wt%, the ion conductivity of the separator increased from 0.300 mS cm^{-1} to 1.679 mS cm^{-1}, and the thin film exhibited good thermal stability, with a 2.3 °C increase in melting point compared to neat PVDF. Also, the tensile strength and Young's modulus significantly increased by 168% and 172%, respectively.

3.3.1.3 Additives in electrolyte and gel-polymer Electrolyte.

Due to its 2D nanosheet structure, alkylammonium ion spacing/coupling agents and PVDF-HFP copolymers could be intercalated in the planar layers of MMT.[231] The prepared solid polymer electrolytes (SPEs) demonstrated good ion conductivity (e.g., 10^{-6} S cm^{-1}), solvent retention capabilities, and dimensional stability. Subsequently, Park et al.[232,233] separately introduced lithium-ion and organically modified MMT in PEO-based electrolytes. The addition of MMT in both cases significantly enhanced the ion conductivity of the electrolyte and effectively reduced the crystallinity of the polymer.

Due to the unique Li$^+$···O–Si interactions present in nano-OMMT, the transfer of Li$^+$ ions within the plastic polymer electrolyte occurred more easily. Consequently, a higher ion conductivity of 1.67×10^{-14} S cm^{-1} and a migration number of 0.67 were achieved. Similar studies were also reported by Cheng et al.[234] about a novel functionalized poly(meta-phenylene isophthalamide) (PMIA)/MMT-based gel polymer electrolyte (GPE) using the electrospinning technique. The well-dispersed MMT fillers within the PMIA membrane could provide an electronegative atmosphere, facilitating the convenient transport of lithium ions across the separator.

3.3.2 Alkali-metal batteries

3.3.2.1 Anode substrate.

Due to the lithiophilic nature of MMT, it holds great potential as a lithium metal anode substrate. Zhu et al.[235] employed MMT-coated copper foil as a robust substrate to promote uniform and stable Li nucleation. The results showed that at 2 mA cm^{-2} and an aerial capacity of 1 mA h cm^{-2}, a Coulombic efficiency as high as 99% was achieved after 700 cycles. Due to the similar properties such as high electronegativity between VMT and MMT, they can effectively adsorb Li$^+$ and facilitate the deposition of Li$^+$. Luo et al.[236] proposed the use of a soft-hard organic–inorganic layered pearl structure to suppress lithium dendrites. In this structure, lithium metal was employed as the soft component, while VMT particles served as the hard inorganic component, exhibiting a 30 times higher theoretical modulus. VMT flakes possess a high negative charge. They can absorb a large number of lithium ions in the electrolyte, and then co-deposit with lithium ions, effectively suppressing the growth of lithium dendrites and forming a branch-free rock-like structure after hundreds of cycles. After the deposition of surface-adsorbed Li$^+$, the VMT flakes regain their negative charge and move away from the substrate along the electric field, facilitating the further absorption of new Li$^+$ ions and enabling uniform deposition in a shuttle-like manner (Fig. 10(a) and (b)).

3.3.2.2 Artificial SEI layer components.

The interlayer spacing of MMT provides a fast pathway for Li$^+$ transport and its inherent lithiophilicity makes it a promising candidate as an artificial SEI layer on lithium metal anodes. Li et al.[240] enhanced the SEI performance and suppressed the growth of dendritic crystals by utilizing Li-ion-modified MMT (Li-MMT),
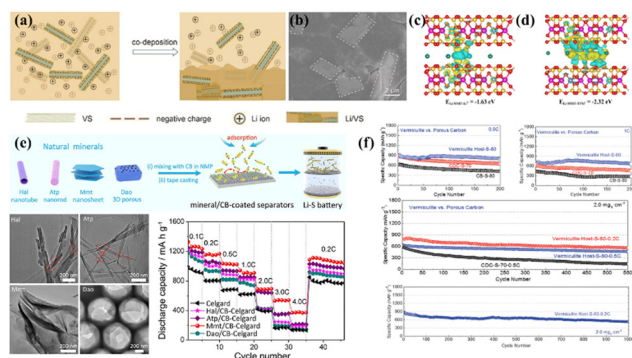
Fig. 10 (a) Schematic illustrating the co-deposition of Li with VS. (b) BSE image of Li plating in EC/DEC electrolyte with 0.1% VS.[236] Copyright 2023, Nonferrous Metals Society of China. Differential charge densities of (c) Li-MMT with TFSI⁻ ions (Li-MMT–TFSI) and (d) Li-MMT with Li⁺ ions (Li-MMT–Li⁺) and the corresponding adsorption energies.[237] Copyright 2021, Wiley-VCH. (e) Schematic illustration of preparation of the mineral/CB-coated separators, transmission electron microscopy (TEM) images of Hal, Atp, Mmt, and Dao, and the rate performance of the Li−S batteries with different separators and the CNT/S cathode.[238] Copyright 2021, Elsevier. (f) Comparison studies of the cycling performance and long-term cycle stability of the VMT−sulfur cathodes with different S contents at the mass loading of 2.0 mg cm⁻².[239] Copyright 2022, Wiley-VCH.

resulting in significant improvements in electrochemical performance. The Li-MMT SEI not only possessed inherent fast Li⁺ channels but also served as a reservoir, providing sufficient lithium ions between and at the edges of the Li-MMT nanoplates for rapid interlayer and intralayer transfer of lithium ions. Furthermore, Shu et al.[241] employed a similar strategy using Li-MMT as an artificial SEI layer, and their research primarily demonstrated that Li-MMT can serve as a single pathway for lithium ions, inhibiting the transport of TFSI⁻ anions within the MMT layer and alleviating the concentration gradient of Li⁺ at the interface (Fig. 10(c) and (d)). Zhang et al.[237] proposed the use of an Ag-montmorillonite (AMMT) interlayer Li⁺ conductor as an interface ion transport precision flow pump to induce rapid and reversible electrodeposition/stripping of Li metal. The negatively charged layer and inherent channels of the AMMT pump could reduce the nucleation barrier and facilitate Li⁺ transport.

A VMT nanosheet-based organic–inorganic hybrid film showed a similar effect in suppressing dendritic growth and mitigating volume fluctuations.[242] The reason for the improvement is related to the mechanical strength of the VN layer.

3.3.2.3 Separator additives. 2D inorganic non-conductive materials can be used as additives to improve the performance of separators in batteries. He et al. incorporated clay with atomic interlayer ion channels in a polymer separator using the electrophoretic deposition technique.[243] Due to the strong adsorption energy between Li-MMT and PVDF-HFP, the Li-MMT/PVDF-HFP membrane exhibited significantly improved electrolyte wettability, thermal stability, mechanical strength, and electrochemical performance. The parallel ion channels with unified Li⁺ flow direction led to the uniform deposition of

lithium ions, resulting in dendrite-free lithium anodes. Wang et al. coated lithium-modified MMT (Li-MMT) onto a porous PP membrane.[244] Li-MMT facilitated a unified flow direction of lithium ions, resulting in the uniform deposition of lithium ions on the anode surface and suppression of lithium dendrite formation. A similar enhancement by MMT nanosheets as an additive was found in PVDF/PAN/VMT[245] and PP/VMT[246] in polymer separators.

3.3.2.4 Additives in electrolyte and gel-polymer electrolyte. In addition, MMT can also function as an additive in liquid electrolytes. Yan et al.[247] introduced MMT as a nucleophilic medium into the host electrolyte to modulate the ion distribution of lithium dendrite deposition. The redistribution of lithium ions effectively suppressed the formation of ion-depleted zones on the anode surface by increasing the ion concentration at the electrode/electrolyte interface, further delaying the occurrence of dendritic growth. As the deposition process proceeded, MMT served as heterogeneous nucleating seeds for Li ion adsorption, promoting uniform deposition instead of large clusters or lithium dendrites.

Also, MMT can be used as a functional additive in quasi-solid-state electrolytes.[261] For example, Park et al.[248] designed a UV-crosslinked nanocomposite polymer–clay solid electrolyte (U-CPCE). The addition of MMT not only altered the local crystallinity of the polymer matrix, increasing the amorphous region for ion conduction, but also intervened in the ion–ion and ion-polymer interactions, enhancing the carrier concentration. It played a crucial role in improving the ion conductivity and facilitating Li⁺ migration, thus resulting in an excellent electrochemical battery performance. Ding et al.[249] designed and fabricated a novel composite solid electrolyte (CMP/MMT), which was composed of a robust interpenetrating polymer network matrix and layered MMT flakes. The ion transport pathways were well connected, allowing full access to the active materials. The addition of MMT not only enhanced the room temperature ionic conductivity and Li⁺ migration number but also provided mechanical support to the soft polymer network, effectively preventing short circuits under mechanical deformation, thereby exhibiting an excellent electrochemical performance. Salot et al.[250] incorporated MMT as an inorganic filler in a PVDF-HFP-based gel electrolyte, resulting in an electrolyte with high ion conductivity (0.48 mS cm⁻¹ at 25 °C) and excellent thermal stability up to 140 °C.

VMT nanosheets can work as additives in polymer-based electrolyte. He et al.[251] prepared VMT nanosheets (VNs) with abundant cation vacancies and incorporated them into a PEO/PVdF-HFP blend polymer electrolyte. The cation vacancies not only provided additional Lewis acid–base interaction sites for lithium ions but also protected the PEO chains from excessive lithium ion oxidation, thereby enhancing the dissociation of lithium salt and the hopping mechanism of lithium ions. Luo et al.[252] investigated vertically aligned two-dimensional VMT nanosheets (VAVS) as advanced fillers for solid polymer electrolytes (SPE), exhibiting enhanced ion conductivity, Li⁺ transference

number, mechanical modulus, and electrochemical stability. Jiang et al.[253] investigated a layered ionic liquid composite electrolyte (L-ILCE) by encapsulating an ionic liquid (IL) within the ordered interlayer nanochannels of a VMT framework. Within the nanochannels, the fine microstructure induced the rearrangement and crystallinity of the ionic crystals, endowing L-ILCE with the combined advantages of liquid electrolytes and solid electrolytes. L-ILCE exhibited high ion conductivity (0.09–1.35×10^{-3} S cm^{-1} in the range of $-40\ ^\circ$C to $100\ ^\circ$C), while polymers and inorganic electrolytes typically lose their ion conductivity below $0\ ^\circ$C.

3.3.4 Alkali–S batteries. The interaction between 2D MMT nanosheets and polysulfides can restrain the shuttle effect of polysulfides because Si–OH groups as Lewis acid sites can form bonds with polysulfides, which effectively inhibits the diffusion of polysulfides to the anode.[254] Furthermore, benefiting from the interlayer cation exchangeability of MMT, the following researchers developed various ion-intercalated MMTs to change the charge of MMT. Specifically, carbon-intercalated MMT (MMT@C),[90] Li-MMT,[244,255–257] and FeS$_2$-intercalated MMT (FeS$_2$@MMT)[91] were developed. Among them, Li-MMT is more widely applied due to the presence of lithium ions in its interlayers, which facilitates faster Li$^+$ transport within the material. Zhang et al.[238] utilized naturally occurring minerals with 1D to 3D microstructures as advanced separators for Li–S batteries. The cell using the MMT/CB-Celgard separator exhibited the highest upper plateau discharge capacity (369 mA h g^{-1}), initial reversible capacity (1496 mA h g^{-1} at 0.1C), rate performance, and cycling stability (666 mA h g^{-1} after 500 cycles at 1.0C with a capacity decay of 0.046% per cycle). Even with a high sulfur loading (8.3 mg cm^{-2}), the MMT/CB-Celgard separator demonstrated stable cycling in Li–S batteries (Fig. 10(e)).

Additionally, MMT is often used in conjunction with other materials possessing different properties. Li et al.[258] developed a multifunctional material composed of MMT and selenium-doped sulfur-polyacrylonitrile (Se$_{0.06}$SPAN) support. MMT provided sufficient channels for Li$^+$ transport, while selenium-doped sulfur-polyacrylonitrile catalyzed the conversion of "dead sulfur" and contributed to the overall capacity.

MMT nanosheets have a better ionic conductivity, thus MMT nanosheets can be combined with materials with high electronic conductivity to provide a fast ion/electron transport. For example, Shao et al.[256] designed a two-dimensional (2D) heterostructure by integrating monolayer lithium-montmorillonite (MMT) with nitrogen-doped rGO. The low diffusion barrier layer on Li-MMT facilitated rapid Li$^+$ transport, while the adjacent RGO constructed a highly conductive electron network, enabling efficient adsorption-diffusion-conversion of polysulfides and achieving fast electrochemical reaction kinetics.

The addition of VMT to the electrode can act as a host for sulfur loading to confine elemental sulfur and immobilize polysulfides, resulting in an enhanced rate and cycling performance.[239] Compared to conventional carbon-sulfur composite materials, the VMT-sulfur composites demonstrated an improved rate performance and enhanced cycling stability (Fig. 10(f)).

VMT in Li–S batteries. VMT-based separators can inhibit the diffusion of polysulfides on the separator through electrostatic interactions and spatial hindrance.[259] Meanwhile, the inorganic thin flakes with high strength and Young's modulus can prevent the penetration of metallic lithium dendrites, resulting in improved safety in the battery. Wang et al.[260] prepared a thin film composite solid electrolyte (LCSE), namely Vr/PEO-LCSE, by filtering VMT nanosheets, and subsequently embedding PEO–LiTFSI in the interlayer *via* an expansion filtration method. The continuous interlayer channels exhibited favorable PEO chain mobility and LiTFSI dissociation, resulting in an ion conductivity of 1.22×10^{-5} S cm^{-1} at $25\ ^\circ$C for Vr/PEO-LCSE.

Tables 1 and 2 summarize the application of 2D inorganic non-conductive materials in alkali metal-based batteries. Overall, these materials can be used as additives for the SEI building block, separators and electrode substrate to improve the electrochemical performance of alkali metal-based batteries.

3.4 Challenges and outlook

The application of 2D inorganic non-conductive materials in enhancing the performance of alkali metal-based batteries has achieved certain success, but there are still many challenges that need to be carefully considered.[262] Firstly, inexpensive methods for producing high-quality 2D materials on a large scale are still lacking at present. For example, it has been reported that the industrial-scale efficiency to prepare BN nanosheets *via* the exfoliation of BN bulk material is less than 30%.[263] Moreover, many 2D inorganic nanosheets are prepared by exfoliation of the corresponding bulk layered materials. Consequently, defects and/or impurities can be introduced in 2D inorganic materials during their preparation. Thus, it is highly desirable to develop novel methods to prepare inorganic nanosheets on a large scale.[264] Secondly, it remains a significant challenge to synthesize the 2D inorganic materials with a controllable microstructure. Thus, the optimization of the microstructure of 2D inorganic materials including surface functional groups and number of nanosheet layers should be carried out to realize desirable properties. Thirdly, it is still a great challenge to fine-control the electrode functionalities by using 2D materials or assemblies of 2D materials in battery systems because the electrochemical performance of batteries is affected by many factors.[265] After the introduction of 2D materials in battery system, new surfaces and/or interfaces are formed among the electrode components. As is known, the surface and interface in the electrode strongly affect the mass transport, charge transfer and ion diffusion in batteries. Thus, further studies on the effects of 2D inorganic materials on the electrode should be performed systematically, especially the relationship between the interfacial properties of inorganic nano-sheets and their functionalities as additives at the atomic level. Finally, it is very important to develop new 2D non-conductive materials with new structures and properties to fulfil the requirements in multiple fields in the future.

Table 1 The application of 2D inorganic non-conductive materials as additives in alkali-ion/S batteries

Material	Additives	Capacity	Rate capacity	Cycling stability	Ref.
1. BN					
rGO/BN thin film	LIBs-anode	At 0.1 A g^{-1}, 278 mA h g^{-1}	At 1 A g^{-1}, 121 mA h g^{-1}	About 100%, 200 cycles	98
MOF-5/BNNs	LIBs-anode	At 0.1A g^{-1}, 1050 mA h g^{-1}	At 2 A g^{-1}, 409 mA h g^{-1}	About 100%, 1000 cycles	99
PVH–LaO/PVH-BN	LIBs-separator	At 0.5C, 158 mA h g^{-1} (Based on LFP)	At 20C, 78 mA h g^{-1}	96%, 1500 cycles	104
PE-BN/PVDF-HFP	LIBs-separator	At 2C, 120 mA h g^{-1} (Based on LFP)	At 4C, 108 mA h g^{-1}	95%, 500 cycles	101
v-BN	Li–S-cathode	At 0.2C, 1262 mA h g^{-1} (1C = 1675 mA g^{-1})	At 1C, 699 mA h g^{-1}	58%, 500 cycles	130
BN/graphene	Li–S-cathode	At 0.1C, 1553 mA h g^{-1}	At 2C, 914 mA h g^{-1}	90%, 500 cycles	132
FBN/graphene	Li–S-cathode	At 0.2C, 1125 mA h g^{-1}	At 6C, 556 mA h g^{-1}	93%, 1000 cycles	133
S-BN@rGO	Li–S-cathode	At 0.2C, 1137 mA h g^{-1}	At 5C, 523 mA h g^{-1}	73%, 500 cycles	135
BN/CNTs	Li–S-cathode	At 0.2C, 1374 mA h g^{-1}	At 4C, 840 mA h g^{-1}	77%, 500 cycles	136
f-BNNS/f-CNTs	Li–S-cathode	At 0.2C, 1136 mA h g^{-1}	At 5C, 430 mA h g^{-1}	Above 100%, 500 cycles	137
BN-carbon separator	Li–S-separator	At 0.5C, 1018 mA h g^{-1}	At 4C, 780 mA h g^{-1}	76%, 250 cycles	139
FBN separator	Li–S-separator	At 0.2C, 1486 mA h g^{-1}	At 7C, 718 mA h g^{-1}	89%, 1000 cycles	140
BN-P@GO	Li–S-separator	At 0.2C, 1092 mA h g^{-1}	At 3C, 626 mA h g^{-1}	59%, 500 cycles	141
CoB/BN@rGO	Li–S-separator	At 0.35 mA cm^{-2}, 1450 mA h g^{-1}	At 8.7 mA cm^{-2}, 480.2 mA h g^{-1}	77%, 700 cycles	142
BN/SWCNT	Li–S-separator	At 0.1C, 1124 mA h g^{-1}	—	—, 100 cycles	113
P-BNNS-PP	Li–S-separator	At 0.3C, 1429 mA h g^{-1}	—	85%, 200 cycles	138
BN doped Li$_7$P$_3$S$_{11}$	Li–S-SSEs	At 0.05C, 803 mA h g^{-1}	—	22%, 50 cycles	143
BN-PEO-PVDF	Li–S-SSEs	At 0.05C, 1000 mA h g^{-1}	At 0.5C, 400 mA h g^{-1}	—, 50 cycles	144
2. g-C$_3$N$_4$					
Li$_4$Ti$_5$O$_{12}$/g-C$_3$N$_4$	LIBs-anode	At 0.2C, 174.8 mA h g^{-1} (1C = 175 mA h g^{-1})	At 3.2C, 142.1 mA h g^{-1}	87%, 500 cycles	147
g-C$_3$N$_4$/MoS$_2$/ZnS	LIBs-anode	At 0.5 A g^{-1}, 900 mA h g^{-1}	At 6 A g^{-1}, 298 mA h g^{-1}	99%, 500 cycles	148
MoS$_2$/g-C$_3$N$_4$	LIBs-anode	At 0.05C, 2467 mA h g^{-1} (1C = 1A g^{-1})	—	48%, 200 cycles	149
SnO$_2$@C$_3$N$_4$	LIBs-anode	156 mA g^{-1}, 995 mA h g^{-1}	3943 mA g^{-1}, 329 mA h g^{-1}	57%, 100 cycles	150
SnS$_2$/g-C$_3$N$_4$/graphite	LIBs-anode	At 1A g^{-1}, 571 mA h g^{-1}	At 5 A g^{-1}, 470 mA h g^{-1}	99.3%, 470 cycles	151
ZnS/g-C$_3$N$_4$	L/SIBs-anode	At 0.1 A g^{-1}, 920 mA h g^{-1} (LIB) At 0.1 A g^{-1}, 501 mA h g^{-1} (LIB)	At 1 A g^{-1}, 612 mA h g^{-1} (LIBs) At 0.1 A g^{-1}, 920 mA h g^{-1} (LIB)	—, 200 cycles —, 100 cycles	152
SnS$_2$@g-C$_3$N$_4$	LIBs-anode	At 50 mA g^{-1}, 736 mA h g^{-1}	At 500 mA g^{-1}, 736 mA h g^{-1}	—, 600 cycles	153
SnO$_2$/g-C$_3$N$_4$	LIBs-anode	At 0.1C, 733 mA h g^{-1}	—	—, 60 cycles	154
SnO$_2$/GO/g-C$_3$N$_4$	LIBs-anode	At 0.1C, 1456 mA h g^{-1}	—	—, 100 cycles	155
Sn/g-C$_3$N$_4$	LIBs-anode	At 100 mA g^{-1}, 592 mA h g^{-1}	At 500 mA g^{-1}, 420 mA h g^{-1}	53%, 100 cycles	156
NiCo$_2$O$_4$/g-C$_3$N$_4$	LIBs-anode	At 100 mA g^{-1}, 1367 mA h g^{-1}	At 1000 mA g^{-1}, 452 mA h g^{-1}	78%, 100 cycles	157
CuO@Cu/g-C$_3$N$_4$	LIBs-anode	At 0.1C, 777 mA h g^{-1}	At 2C, 450 mA h g^{-1}	—, 625 cycles	158
MoO$_x$/UCN	LIBs-anode	At 0.1 A g^{-1}, 1069 mA h g^{-1}	At 2A g^{-1}, 703 mA h g^{-1}	70%, 100 cycles	159
g-C$_3$N$_4$/WS$_2$	LIBs-anode	At 0.1C, 655.7 mA h g^{-1}	At 2C, 247.4 mA h g^{-1}	68.7%, 200 cycles	160
g-C$_3$N$_4$@RGO	LIBs-anode	At 50 mA g^{-1}, 911 mA h g^{-1}	At 800 mA g^{-1}, 666 mA h g^{-1}	—, 1000 cycles	161
P/rGO-C$_3$N$_4$	LIBs-anode	At 200 mA g^{-1}, 1806 mA h g^{-1}	At 1000 mA g^{-1}, 855 mA h g^{-1}	—, 600 cycles	162
CuCo$_2$O$_4$@g-C$_3$N$_4$	LIBs-anode	At 0.1 A g^{-1}, 577 mA h g^{-1}	At 2 A g^{-1}, 499 mA h g^{-1}	76%, 60 cycles	163
Co$_{1-x}$S@g-C$_3$N$_4$	LIBs-anode	At 0.1 A g^{-1}, 789 mA h g^{-1}	—	—, 210 cycles	164
Se-H-g-C$_3$N$_4$	LIBs-anode	At 0.1 A g^{-1}, 814 mA h g^{-1}	At 2 A g^{-1}, 544 mA h g^{-1}	54%, 1000 cycles	165
g-C$_3$N$_4$/Mo$_2$CT$_x$	LIBs-anode	At 0.1 A g^{-1}, 606 mA h g^{-1}	At 2 A g^{-1}, 257 mA h g^{-1}	97%, 1800 cycles	166
C/g-C$_3$N$_4$	SIBs-anode	At 0.1 A g^{-1}, 254 mA h g^{-1}	At 1 A g^{-1}, 151 mA h g^{-1}	—, 400 cycles	167
crystalline C$_3$N$_4$/C	SIBs-anode	At 0.1 A g^{-1}, 286 mA h g^{-1}	At 3.2 A g^{-1}, 151 mA h g^{-1}	—, 2000 cycles	168
Graphite/g-C$_3$N$_4$ heterojunction	SIBs-anode	At 0.1 A g^{-1}, 285 mA h g^{-1}	At 1 A g^{-1}, 111 mA h g^{-1}	—, 10 000 cycles	169
SnS$_2$@g-C$_3$N$_4$	SIBs-anode	At 50 mA g^{-1}, 901 mA h g^{-1}	At 2000 mA g^{-1}, 610 mA h g^{-1}	123%, 400 cycles	170
1D/2D C$_3$N$_4$/rGO	KIBs-anode	At 0.1 A g^{-1}, 464 mA h g^{-1}		—, 1000 cycles	171
PCN/rGO	Li–S-cathode	At 0.1C, 1205 mA h g^{-1}	At 5C,483 mA h g^{-1}	61%, 800 cycles	194
3D Porous S/graphene@g-C$_3$N$_4$	Li–S-cathode	At 0.5C, 1116 mA h g^{-1}	At 5C, 828 mA h g^{-1}	86%, 800 cycles	195
rGO/g-C$_3$N$_4$/CNT	Li–S-cathode	At 0.05C, 1263 mA h g^{-1}	At 2C, 554 mA h g^{-1}	85%, 500 cycles	178
S/g-C$_3$N$_4$	Li–S-cathode	At 0.2C, 1018 mA h g^{-1}	At 5C, 607 mA h g^{-1}	72%, 300 cycles	196
g-C$_3$N$_4$/graphene	Li–S-cathode	At 0.2C, 1098 mA h g^{-1}	At 2C, 631 mA h g^{-1}	—, 1000 cycles	197
g-C$_3$N$_4$/CNT	Li–S-separator	At 0.2C, 870 mA h g^{-1}	At 2C, 755 mA h g^{-1}	85%, 500 cycles	199
Fe/Co-C$_3$N$_4$/C/S	Li–S-cathode	At 0.1C, 1257 mA h g^{-1}	At 2C, 453 mA h g^{-1}	78%, 135 cycles	200
Ti$_x$O$_y$–Ti$_3$C$_2$/C$_3$N$_4$	Li–S-cathode	At 0.5C, 749 mA h g^{-1}	—	56%, 2000 cycles	201
MXene/g-C$_3$N$_4$	Li–S-cathode	At 1C, 718 mA h g^{-1}	At 4C, 632 mA h g^{-1}	59%, 500 cycles	205
MoS$_2$/g-C$_3$N$_4$	Li–S-cathode	At 0.5C, 925 mA h g^{-1}	At 8C, 472 mA h g^{-1}	73%, 500 cycles	207
g-C$_3$N$_4$/g-C$_3$N$_4$ Heterojunction	Li–S-cathode	At 1C, 640 mA h g^{-1}	—	67%, 150 cycles	208
Ni–C$_3$N$_4$/C	Li–S-separator	At 0.1 A g^{-1}, 1253 mA h g^{-1}	At 2 A g^{-1}, 835 mA h g^{-1}	89%, 300 cycles	209
FeOOH/coated g-C$_3$N$_4$/KB	Li–S-separator	At 0.1C, 1246 mA h g^{-1}	At 2C, 802 mA h g^{-1}	50%, 900 cycles	210
Co-doped g-C$_3$N$_4$	Li–S-separator	At 0.2C, 1121 mA h g^{-1}	At 2C, 529 mA h g^{-1}	95%, 250 cycles	211
Graphene@g-C$_3$N$_4$	Li–O-catalyst	0.2 mA cm^{-1}, 17 300 mA h g^{-1}	0.4 mA cm^{-1}, 1000 mA h g^{-1}	—, 105 cycles	212
Pt@g-C$_3$N$_4$	Li–O-catalyst	At 0.2 A g^{-1}, 13 843 mA h g^{-1}	At 0.8 A g^{-1}, 5964 mA h g^{-1}	—, 100 cycles	218

Table 1 (*continued*)

Material	Additives	Capacity	Rate capacity	Cycling stability	Ref.
3. MMT					
MMT/carbon	LIBs-anode	At 0.02 A g^{-1}, 1432 mA h g^{-1}	—	—, 50 cycles	223
MCMB@MMT	DIBs-anode	At 2C, $\sim$ 80 mA h g^{-1}	—	100%, 1000 cycles	88
MMT/P(VdF-TrFE)	LIBs-separator	At 0.1C, 119 mA h g^{-1}	At 1C, 86 mA h g^{-1}	—	226
PVDF/MMT	LIBs-separator	At 0.2C, 138 mA h g^{-1}	At 1C, 128 mA h g^{-1}	100%, 50 cycles	227
5 M/P-PMIA	LIBs-gel polymer electrolyte	At 2C, 140 mA h g^{-1}	—	89%, 200 cycles	234
MMT@C@PP	Li–S-separator	At 0.5 mA cm^{-1}, 1049 mA h g^{-1}	At 3 mA cm^{-1}, 684 mA h g^{-1}	90%, 300 cycles	90
Co/N-C@Li-MMT	Li–S-separator	At 0.1C, 1275 mA h g^{-1}	At 2C, 656 mA h g^{-1}	—, 100 cycles	255
MMT/RGO-PP	Li–S-separator	At 0.1C, 1389 mA h g^{-1}	At 3C, 848 mA h g^{-1}	47%, 800 cycles	256
PPY/Li-MMT	Li–S-separator	At 0.2 mA cm^{-1}, 1226 mA h g^{-1}	At 5 mA cm^{-1}, 540 mA h g^{-1}	—, 500 cycles	257
FeS$_2$@MMT	Li–S-separator	At 0.2C, 1168 mA h g^{-1}	At 10C, 358 mA h g^{-1}	69%, 1000 cycles	91
Mmt/carbon black	Li–S-separator	At 0.1C, 1496 mA h g^{-1}	At 3C, 541 mA h g^{-1}	77%, 500 cycles	238
Se$_{0.06}$SPAN/MMT@PP	Li–S-separator	At 0.1C, 1454 mA h g^{-1}	At 5C, 670 mA h g^{-1}	66%, 1000 cycles	258
4. VMT					
VMT/PP	LIBs-separator	At 0.1C, 148 mA h g^{-1} (LFP)	—	—, 25 cycles	229
PVDF/VMT/LPT	LIBs-separator	At 0.5C, 161 mA h g^{-1} (LFP)	—	98%, 100 cycles	225
PVDF/VMT	LIBs-separator	At 0.2C, 155 mA h g^{-1} (LFP)	At 2C, 119 mA h g^{-1} (LFP)	95%, 100 cycles	230
2D vermiculite separator	Li–S-separator	At 0.1C, 1000 mA h g^{-1}	At 2C, 600 mA h g^{-1}	—, 50 cycles	259
Vr/PEO-LCSE	Li–S-SSEs	At 0.05C, 1252 mA h g^{-1}	At 0.2C, 1000 mA h g^{-1}	—, 150 cycles	260

Table 2 The application of 2D inorganic non-conductive materials as additives in alkali-metal batteries

Material	Additives in battery system	Electrochemical performance		Ref.
		Half-cell (current density & capacity; cycling life; CE)	Symmetric cell (current density & capacity; cycling life)	
1. BN				
LHC/BN	LMBs-anode	1 mA cm^{-2}, 1 mA h cm^{-2} 500 cycles; 98.5%	1 mA cm^{-2}, 1 mA h cm^{-2}; 700 h	105
h-BN/Zn–Li alloy	LMBs-anode	—	2 mA cm^{-2}, 2 mA h cm^{-2}; 600 h	106
Li-BNNS	LMBs-anode	—	0.3 mA cm^{-2}, 0.15 mA h cm^{-2}; 380 h	107
h-BN on Cu	LMBs-artificial SEI layer	0.5 mA cm^{-2}, 1 mA h cm^{-2} 50 cycles; 97%	—	109
Hierarchical h-BN protective layer	LMBs-artificial SEI layer	—	1 mA cm^{-2}, 1 mA h cm^{-2}; 1700 h	110
BN/inorganics/rGO	LMBs-artificial SEI layer	0.5 mA cm^{-2}, 1 mA h cm^{-2} 300 cycles; 98.5%	0.5 mA cm^{-2}, 1 mA h cm^{-2}; 1600 h	111
BN@PP	LMBs-separator	0.5 mA cm^{-2}, 1 mA h cm^{-2} 100 cycles; 92%	—	114
BN/PVDF-HFP	LMBs-separator	0.5 mA cm^{-2}, 0.5 mA h cm^{-2} 90 cycles; 92%	1 mA cm^{-2}, 1 mA h cm^{-2}; 500 h	115
BN coating PP	LMBs-separator	—	5 mA cm^{-2}, 5 mA h; cm^{-2}; 80 h	116
BN nanosheets	LMBs-electrolyte	1 mA cm^{-2}, 1 mA h cm^{-2} 180 cycles; 99%	1 mA cm^{-2}, 1 mA h cm^{-2}; 1500 h	117
2D BN nanoflakes	LMBs-gel polymer electrolyte	—	1 mA cm^{-2}, 1 mA h cm^{-2}; 2000 h	118
PVdF CPE-BN	LMBs-gel polymer electrolyte	—	0.1 mA cm^{-2}, 0.05 mA h cm^{-2}; 2000 h	119
h-BN enhanced PVDF-based CPE	LMBs-gel polymer electrolyte	—	0.1 mA cm^{-2}, —; 1200 h	120
BNNS/PEO	LMBs-polymer solid-state electrolyte	—	0.3 mA cm^{-2}, —; 750 h	112
PEO/LiTFSI/SiO$_2$@BNNS	LMBs-polymer solid-state electrolyte	—	0.4 mA cm^{-2}, —; 1000 h	121
PEO/LiTFSI/h-BN	LMBs-polymer solid-state electrolyte	—	0.2 mA cm^{-2}, —; 430 h	122
ANF-PEO-BN	LMBs-polymer solid-state electrolyte	—	0.1 mA cm^{-2}, 0.2 mA h cm^{-2}; 3250 h	123
BN/LATP/BN	LMBs-solid-state electrolyte	—	0.3 mA cm^{-2}, —; 3250 h	126
BNRA-LATP	LMBs-solid-state electrolyte	—	0.05 mA cm^{-2}, —; 1200 h	127
PVDF-HFP/LALZO/h-BN	LMBs-solid-state electrolyte	—	2 mA cm^{-2}, —; 1000 h	128
2. g-C$_3$N$_4$				
g-C$_3$N$_4$@Ni foam	LMBs-anode	2 mA cm^{-2}, 1 mA h cm^{-2} 300 cycles; 98%	1 mA cm^{-2}, 1 mA h cm^{-2}; 900 h	174
rGO-C$_3$N$_4$	LMBs-anode	1 mA cm^{-2}, 1 mA h cm^{-2} 300 cycles; 96.6%	1 mA cm^{-2}, 1 mA h cm^{-2}; 1700 h	175

Table 2 (continued)

Material	Additives in battery system	Electrochemical performance		Ref.
		Half-cell (current density & capacity; cycling life; CE)	Symmetric cell (current density & capacity; cycling life)	
Graphitic C_3N_4	LMBs-anode	1 mA cm^{-2}, 1 mA h cm^{-2} 40 cycles; —	1 mA cm^{-2}, 1 mA h cm^{-2}; 400 h	179
g-C_3N_4/CC	LMBs-anode	—	2 mA cm^{-2}, —; 1500 h	176
g-C_3N_4/Ti$_3$C$_2$T$_x$	LMBs-anode	0.5 mA cm^{-2}, 1 mA h cm^{-2} 400 cycles; 98.4%	0.5 mA cm^{-2}, 0.5 mA h cm^{-2}; 1100 cycles	180
LiH&Li$_3$N@g-C_3N_4	LMBs-anode	—	1 mA cm^{-2}, 1 mA h cm^{-2}; 1100 h	181
Acid-treated g-C_3N_4	LMBs-artificial SEI layer	—	1 mA cm^{-2}, 1 mA h cm^{-2}; 2100 h	182
P doped C_3N_4	LMBs-anode	—	2 mA cm^{-2}, 2 mA h cm^{-2}; 800 h	177
LiTFSI-DGM-C_3N_4	LMBs-polymer electrolyte	—	0.5 mA cm^{-2}, 1.5 mA h cm^{-2}; 580 h	183
g-C_3N_4@PVDF-HEP	LMBs-solid polymer electrolyte	—	0.05 mA cm^{-2}, 0.1 mA h cm^{-2}; 1000 h	184
PVDF-HFP/LATP/g-C_3N_4	LMBs-composite polymer electrolyte	—	0.1 mA cm^{-2}, —; 200 h	185
g-C_3N_4/LATP/ PVDF	LMBs-composite polymer electrolyte	—	0.1 mA cm^{-2}, —; 740 h	186
g-C_3N_4 modified PEO electrolyte	LMBs-solid polymer electrolyte	—	0.1 mA cm^{-2}, —; 900 h	187
PEO/porous g-C_3N_4/LiTFSI	LMBs-solid polymer electrolyte	—	0.1 mA cm^{-2}, —; 1400 h	188
LLZO/ g-C_3N_4	LMBs-solid-state electrolyte	—	0.1 mA cm^{-2}, —; 1500 h	190
3. MMT				
MMT@Cu	LMBs-anode	2 mA cm^{-2}, 1 mA h cm^{-2} 700 cycles; 98.4%	1 mA cm^{-2}, 1 mA h cm^{-2}; 20 000 min	235
Li-MMT	LMBs-artificial SEI layer	0.5 mA cm^{-2}, 0.5 mA h cm^{-2} 400 cycles; 98.4%	0.5 mA cm^{-2}, 0.5 mA h cm^{-2}; 1000 h	240
Single-ion-conducting Li-MMT	LMBs-artificial SEI layer	—	0.5 mA cm^{-2}, 0.5 mA h cm^{-2}; 1300 h	241
Ag-MMT	LMBs-artificial SEI layer	1 mA cm^{-2}, 1 mA h cm^{-2} 400 cycles; 97.5%	1 mA cm^{-2}, 1 mA h cm^{-2}; 2500 h	237
Li-MMT/PVDF-HFP	LMBs-separator	—	0.5 mA cm^{-2}, —; 300 h	243
Li-MMT/PP	LMBs-separator	1 mA cm^{-2}, 1 mA h cm^{-2} 200 cycles; 98.2%	1 mA cm^{-2}, 1 mA h cm^{-2}; 800 h	244
MMT	LMBs-electrolyte additive	0.5 mA cm^{-2}, 0.5 mA h cm^{-2} 300 cycles; 98%	1 mA cm^{-2}, —; 1200 h	247
ETPTA/PVdF-HFP/MMT	LMBs-composite polymer electrolyte	—	0.5 mA cm^{-2}, —; 500 h	248
CMP/MMT	LMBs-solid polymer electrolyte	0.2 mA cm^{-2}, 0.2 mA h cm^{-2} 300 cycles; 96%	0.2 mA cm^{-2}, 0.2 mA h cm^{-2}; 1200 h	249
4. VMT				
VMT flakes	LMBs-anode	—	1 mA cm^{-2}, 1 mA h cm^{-2}; 600 h	236
Dual-layer VMT hybrid film	LMBs-artificial SEI layer	—	1 mA cm^{-2}, 1 mA h cm^{-2}; 670 h	242
PVdF/PAN/VMT	LMBs-separator	—	1 mA cm^{-2}, 2 mA h cm^{-2}; 600 h	245
Vermiculite composite separator	LMBs-separator	1 mA cm^{-2}, 1 mA h cm^{-2} 300 cycles; 98.1%	2 mA cm^{-2}, 1 mA h cm^{-2}; 500 h	246
VNs filled PEO-based GPE	LMBs-gel polymer electrolyte	—	1 mA cm^{-2}, —; 1000 h	251
VAVS-CSPE	LMBs-solid polymer electrolyte	—	0.5 mA cm^{-2}, 0.083 mA h cm^{-2} 1300 h	252

4. Conclusions

In this review, we summarized the recent progress in the application of two-dimensional inorganic non-conductive materials in alkali metal-based batteries. Due to their excellent specific surface area and unique physical/chemical properties, two-dimensional inorganic materials have shown great potential in alkali metal-based batteries. Their non-conductive nature and special properties allow them to be applied not only as additives in electrode materials but also in separators, artificial protective layers, and solid-state electrolytes. In this review, we provided a detailed account of the research progress on these materials as electrode materials or additives in alkali metal-based batteries, as well as their applications as separators, substrates for lithium/sodium/potassium metal anodes, anchoring materials in Li–S batteries, and catalytic materials in Li–O batteries.

The characteristics of two-dimensional inorganic non-conductive materials endow them with great potential for further development. For instance, the abundant adsorption sites in BN and g-C_3N_4 for alkali metal ions make them excellent additives for alkali metal-based ion batteries. Also, due to the exceptional film-forming properties of two-dimensional materials, they can even replace binders and directly form independent thin films with the electrode materials. Moreover, the excellent mechanical properties, thermal stability, and ion transport properties of two-dimensional inorganic materials make them promising candidates as separator additives and protective layers for alkali metal-based battery anodes. The addition of materials such as BN and g-C_3N_4 can effectively reduce the crystallinity of polymer electrolytes and enhance the ion transport. Additionally, their strong anchoring and oxygen reduction capabilities make them excellent main materials or additives for sulfur cathodes and air electrodes.

In summary, the application of two-dimensional inorganic non-conductive materials in lithium metal-based batteries has been widely studied, but their application in sodium/potassium metal-based batteries still needs to be further studied. There are still many obstacles to be overcome from laboratory research to industrial production. Two-dimensional inorganic non-conductive materials offer new choices for constructing components of alkali metal-based batteries and show potential to contribute to a better battery performance. In the future, it is expected that alkali metal-based batteries with a higher capacity, higher rate performance, longer cycle life, and lower cost will be achieved by optimizing the present 2D materials and developing novel 2D materials.

Author contributions

Yuxi Shen, writing original draft. Zengquan Zhu, data preparation. Zhefeng Xu, supervision. Yueming Li, supervision, writing – review & editing, project administration.

Data availability

No primary research results, software or code have been included and no new data were generated or analysed as part of this review.

Conflicts of interest

There are no conflicts to declare.

Acknowledgements

Notes and references

1 W. Zhang, Y. Huang, Y. Liu, L. Wang, S. Chou and H. Liu, *Adv. Energy Mater.*, 2019, **9**, 1900464.

2 W. Cao, Q. Li, X. Yu and H. Li, Controlling Li deposition below the interface, *eScience*, 2022, **2**, 47–78.

3 J. Y. Wei, X. Q. Zhang, L. P. Hou, P. Shi, B. Q. Li, Y. Xiao, C. Yan, H. Yuan and J. Q. Huang, *Adv. Mater.*, 2020, **32**, 2003012.

4 C. Shu, J. Wang, J. Long, H. K. Liu and S. X. Dou, *Adv. Mater.*, 2019, **31**, 1804587–1804630.

5 C. Yang, S. Xin, L. Mai and Y. You, *Adv. Energy Mater.*, 2020, **11**, 2000974.

6 Y. Sun, J.-C. Li, H. Zhou and S. Guo, Wide-temperature-range sodium-metal batteries: from fundamentals and obstacles to optimization, *Energy Environ. Sci.*, 2023, **16**, 4759–4811.

7 X. Min, J. Xiao, M. Fang, W. Wang, Y. Zhao, Y. Liu, A. M. Abdelkader, K. Xi, R. V. Kumar and Z. Huang, *Energy Environ. Sci.*, 2021, **14**, 2186–2243.

8 C. Chu, R. Li, F. Cai, Z. Bai, Y. Wang, X. Xu, N. Wang, J. Yang and S. Dou, *Energy Environ. Sci.*, 2021, **14**, 4318–4340.

9 R. Rajagopalan, Y. Tang, X. Ji, C. Jia and H. Wang, *Adv. Funct. Mater.*, 2020, **30**, 1909486.

10 P. Liu and D. Mitlin, *Acc. Chem. Res.*, 2020, **53**, 1161–1175.

11 A. Ransil and A. M. Belcher, Structural ceramic batteries using an earth-abundant inorganic waterglass binder, *Nat. Commun.*, 2021, **12**, 6494.

12 Y. Shen, Z. Pu, Y. Zhang, Y. Chen, H. Zhang, N. Wang, H. Qiu and Y. Li, *J. Mater. Chem. A*, 2022, **10**, 17199–17207.

13 J. E. ten Elshof, H. Yuan and P. Gonzalez Rodriguez, *Adv. Energy Mater.*, 2016, **6**, 1600355.

14 M. G. Rasul, A. Kiziltas, B. Arfaei and R. Shahbazian-Yassar, *npj 2D Mater. Appl.*, 2021, **5**, 56.

15 J. Wang and S. Wang, *Coord. Chem. Rev.*, 2022, **453**, 21338–21354.

16 Z. Zeng, Y. Dong, S. Yuan, W. Zhao, L. Wang, S. Liu, Y. Yang, P. Ge, W. Sun and X. Ji, *Energy Storage Mater.*, 2022, **45**, 442–464.

17 S. Angizi, S. A. A. Alem, M. Hasanzadeh Azar, F. Shayeganfar, M. I. Manning, A. Hatamie, A. Pakdel and A. Simchi, *Prog. Mater. Sci.*, 2022, **124**, 100884.

18 N. Yaghmaeiyan, M. Mirzaei and R. Delghavi, *Results Chem.*, 2022, **4**, 100549.

19 M. Li, Y. Zhao, Z. Ai, H. Bai, T. Zhang and S. Song, *Chem. Phys.*, 2021, **550**, 111313.

20 S. Angizi, S. A. A. Alem, M. Hasanzadeh Azar, F. Shayeganfar, M. I. Manning, A. Hatamie, A. Pakdel and A. Simchi, *Prog. Mater. Sci.*, 2022, **124**, 100884.

21 W. Paszkowicz, J. B. Pelka, M. Knapp, T. Szyszko and S. Podsiadlo, *Appl. Phys. A: Mater. Sci. Process.*, 2002, **75**, 431–435.

22 N. Izyumskaya, D. O. Demchenko, S. Das, Ü. Özgür, V. Avrutin and H. Morkoç, *Adv. Electron. Mater.*, 2017, **3**, 1600485.

23 G. Cassabois, P. Valvin and B. Gil, *Nat. Photonics*, 2016, **10**, 262–266.

24 N. Marom, J. Bernstein, J. Garel, A. Tkatchenko, E. Joselevich, L. Kronik and O. Hod, *Phys. Rev. Lett.*, 2010, **105**, 046801.

25 S. M. Gilbert, T. Pham, M. Dogan, S. Oh, B. Shevitski, G. Schumm, S. Liu, P. Ercius, S. Aloni, M. L. Cohen and A. Zettl, *2D Mater.*, 2019, **6**, 021006.

26 G. Constantinescu, A. Kuc and T. Heine, *Phys. Rev. Lett.*, 2013, **111**, 036104.

27 A. E. Naclerio and P. R. Kidambi, *Adv. Mater.*, 2022, **35**, 2207374.

28 E. I. Barbara Jürgens, J. Senker, P. Kroll, H. Müller and W. Schnick, *J. Am. Chem. Soc.*, 2003, **125**, 10288–10300.

29 A. Hayat, A. G. Al-Sehemi, K. S. El-Nasser, T. A. Taha, A. A. Al-Ghamdi, S. Jawad Ali Shah, M. A. Amin, T. Ali, T. Bashir, A. Palamanit, J. Khan and W. I. Nawawi, *Int. J. Hydrogen Energy*, 2022, **47**, 5142–5191.

30 Q. Hao, G. Jia, W. Wei, A. Vinu, Y. Wang, H. Arandiyan and B.-J. Ni, *Nano Res.*, 2019, **13**, 18–37.

31 B. He, M. Feng, X. Chen and J. Sun, *Green Energy Environ.*, 2021, **6**, 823–845.

32 N. Rono, J. K. Kibet, B. S. Martincigh and V. O. Nyamori, *Crit. Rev. Solid State Mater. Sci.*, 2021, **46**, 189–217.

33 Y. Lin and J. W. Connell, *Nanoscale*, 2012, **4**, 6908–6939.

34 J. Wen, J. Xie, X. Chen and X. Li, *Appl. Surf. Sci.*, 2017, **391**, 72–123.

35 A. H. Alias, M. N. Norizan, F. A. Sabaruddin, M. R. M. Asyraf, M. N. F. Norrrahim, A. R. Ilyas, A. M. Kuzmin, M. Rayung, S. S. Shazleen, A. Nazrin, S. F. K. Sherwani, M. M. Harussani, M. S. N. Atikah, M. R. Ishak, S. M. Sapuan and A. Khalina, *Coatings*, 2021, **11**, 1355.

36 F. Bergaya, C. Detellier, J. F. Lambert and G. Lagaly, *Handbook of Clay Science*, 2013, pp. 655–677.

37 F. Uddin, *Metall. Mater. Trans. A*, 2008, **39**, 2804–2814.

38 T. Nakato and N. Miyamoto, *Materials*, 2009, **2**, 1734–1761.

39 F. Uddin, *Current Topics in the Utilization of Clay in Industrial and Medical Applications*, 2018.

40 B. S. Kumar, A. Dhakshinamoorthy and K. Pitchumani, *Catal. Sci. Technol.*, 2014, **4**, 2378–2396.

41 W. J. Huang, J. H. Liu, Q. M. She, J. Q. Zhong, G. E. Christidis and C. H. Zhou, *Catal. Rev.*, 2021, **65**, 929–985.

42 J. Feng, M. Liu, L. Fu, S. Ma, J. Yang, W. Mo and X. Su, *Ceram. Int.*, 2020, **46**, 6413–6417.

43 H. F. Muiambo, W. W. Focke, M. Atanasova and A. Benhamida, *Appl. Clay Sci.*, 2015, **105–106**, 14–20.

44 A. N. Nguyen, L. Reinert, J. M. Lévêque, A. Beziat, P. Dehaudt, J. F. Juliaa and L. Duclaux, *Appl. Clay Sci.*, 2013, **72**, 9–17.

45 S. İşçi, *Appl. Clay Sci.*, 2017, **146**, 7–13.

46 H. F. Muiambo and W. W. Focke, *Mol. Cryst. Liq. Cryst.*, 2012, **555**, 65–75.

47 O. Folorunso, C. Dodds, G. Dimitrakis and S. Kingman, *Int. J. Miner. Process.*, 2012, **114–117**, 69–79.

48 K. Okada, S. Matsui, T. Isobe, Y. Kameshima and A. Nakajima, *Ceram. Int.*, 2008, **34**, 345–350.

49 T. T. Zhu, C. H. Zhou, F. B. Kabwe, Q. Q. Wu, C. S. Li and J. R. Zhang, *Appl. Clay Sci.*, 2019, **169**, 48–66.

50 Z. Fu, T. Liu, X. Kong, Y. Liu, J. Xu, B. Zhang, H. Chen and Z. Chen, *Mater. Lett.*, 2019, **238**, 175–178.

51 J.-J. Shao, K. Raidongia, A. R. Koltonow and J. Huang, *Nat. Commun.*, 2015, **6**, 7602.

52 H. Bai, Y. Zhao, W. Wang, T. Zhang, H. Yi and S. Song, *Ceram. Int.*, 2019, **45**, 17054–17063.

53 H. Zhang and Y. Yao, *Environ. Chem. Lett.*, 2017, **15**, 507–513.

54 L. Zang, J. Luo, J. Guo, H. Liu and J. Ru, *Polym. Bull.*, 2010, **65**, 669–680.

55 X. J. Yang, L. L. Li, W. L. Sang, J. L. Zhao, X. X. Wang, C. Yu, X. H. Zhang and C. C. Tang, *J. Alloys Compd.*, 2017, **693**, 642–649.

56 Y. Zhang, M. Wei, Q. Fu and X. Bao, *Sci. Bull.*, 2015, **60**, 1572–1579.

57 Y. Zhang, X. Weng, H. Li, H. Li, M. Wei, J. Xiao, Z. Liu, M. Chen, Q. Fu and X. Bao, *Nano Lett.*, 2015, **15**, 3616–3623.

58 S. Gao, B. Li, D. Li, C. Zhang, R. Liu and S. Wang, *Ceram. Int.*, 2018, **44**, 11424–11430.

59 A. Kuang, T. Zhou, G. Wang, Y. Li, G. Wu, H. Yuan, H. Chen and X. Yang, *Appl. Surf. Sci.*, 2016, **362**, 562–571.

60 J.-S. Li, C.-R. Zhang and B. Li, *Appl. Surf. Sci.*, 2011, **257**, 7752–7757.

61 C. Morchutt, J. Björk, S. Krotzky, R. Gutzler and K. Kern, *Chem. Commun.*, 2015, **51**, 2440–2443.

62 J. Ren, N. Zhang, H. Zhang and X. Peng, *Struct. Chem.*, 2014, **26**, 731–738.

63 S. Roth, F. Matsui, T. Greber and J. Osterwalder, *Nano Lett.*, 2013, **13**, 2668–2675.

64 F. Cao, Y. Ding, L. Chen, C. Chen and Z. Fang, *Mater. Design*, 2014, **54**, 610–615.

65 M. Corso, W. Auwärter, M. Muntwiler, A. Tamai, T. Greber and J. R. Osterwalder, *Science*, 2004, **303**, 217–220.

66 V. Deshmukh, M. Nagnathappa, B. Kharat and A. Chaudhari, *J. Mol. Liq.*, 2014, **193**, 13–22.

67 S. Duperrier, R. Chiriac, C. Sigala, C. Gervais, S. Bernard, D. Cornu and P. Miele, *J. Eur. Ceram. Soc.*, 2009, **29**, 851–855.

68 R. Kumar, S. Sahoo, E. Joanni, R. K. Singh, R. M. Yadav, R. K. Verma, D. P. Singh, W. K. Tan, A. Pérez del Pino, S. A. Moshkalev and A. Matsuda, *Nano Res.*, 2019, **12**, 2655–2694.

69 A. Rice, A. Allerman, M. Crawford, T. Beechem, T. Ohta, C. Spataru, J. Figiel and M. Smith, *J. Cryst. Growth*, 2018, **485**, 90–95.

70 J. Lee, A. V. Ravichandran, J. Mohan, L. Cheng, A. T. Lucero, H. Zhu, Z. Che, M. Catalano, M. J. Kim, R. M. Wallace, A. Venugopal, W. Choi, L. Colombo and J. Kim, *ACS Appl. Mater. Interfaces*, 2020, **12**, 36688–36694.

71 S. Behura, P. Nguyen, S. Che, R. Debbarma and V. Berry, *J. Am. Chem. Soc.*, 2015, **137**, 13060–13065.

72 R. Y. Tay, S. H. Tsang, M. Loeblein, W. L. Chow, G. C. Loh, J. W. Toh, S. L. Ang and E. H. T. Teo, *Appl. Phys. Lett.*, 2015, **106**, 101901.

73 S. Behura, P. Nguyen, R. Debbarma, S. Che, M. R. Seacrist and V. Berry, *ACS Nano*, 2017, **11**, 4985–4994.

74 P. S. J. L. P. A. E. Sutter, *ACS Nano*, 2011, **5**, 7303–7309.

75 H. Huang, L. Jiang, J. Yang, S. Zhou, X. Yuan, J. Liang, H. Wang, H. Wang, Y. Bu and H. Li, *Renewable Sustainable Energy Rev.*, 2023, **173**, 113110.

76 Y. Hong, E. Liu, J. Shi, X. Lin, L. Sheng, M. Zhang, L. Wang and J. Chen, *Int. J. Hydrogen Energy*, 2019, **44**, 7194–7204.

77 J. Wang and S. Wang, *Coord. Chem. Rev.*, 2022, **453**, 214338.

78 A. Hayat, T. A. M. Taha, A. M. Alenad, L. Yingjin, S. K. B. Mane, A. Hayat, M. Khan, A. U. Rehman, W. U. Khan and N. Shaishta, *Energy Technol.*, 2021, **9**, 2100091.

79 A. Hayat, T. A. Taha, A. M. Alenad, T. Ali, T. Bashir, A. Ur Rehman, I. Ullah, A. Hayat, A. Irfan and W. U. Khan, *Int. J. Energy Res.*, 2021, **45**, 19921–19928.

80 A. M. Alenad, T. A. Taha, M. A. Amin, A. Irfan, J. Oliva, Y. Al-Hadeethi, A. Palamanit, M. khan, A. Hayat, S. Kumar Baburao Mane and M. Sohail, *J. Photochem. Photobiol., A*, 2022, **423**, 113591.

81 N. F. F. Moreira, M. J. Sampaio, A. R. Ribeiro, C. G. Silva, J. L. Faria and A. M. T. Silva, *Appl. Catal., B*, 2019, **248**, 184–192.

82 M. Sohail, T. Altalhi, A. G. Al-Sehemi, T. A. M. Taha, K. S. El-Nasser, A. A. Al-Ghamdi, M. Boukhari, A. Palamanit, A. Hayat, M. A. Amin and W. I. Nawawi Bin Wan Ismail, *Nanomaterials*, 2021, **11**, 3245.

83 Y. Liu, X. Guo, Z. Chen, W. Zhang, Y. Wang, Y. Zheng, X. Tang, M. Zhang, Z. Peng, R. Li and Y. Huang, *Appl. Catal., B*, 2020, **266**, 118624.

84 X. Dong and F. Cheng, *J. Mater. Chem. A*, 2015, **3**, 23642–23652.

85 P. Niu, L. Zhang, G. Liu and H.-M. Cheng, *Adv. Funct. Mater.*, 2012, **22**, 4763–4770.

86 Y. Hong, J. Shi, W. Shi, Z. Fang, R. Chen and Y. Huang, *Carbon*, 2018, **136**, 160–167.

87 X. Zhang, X. Xie, H. Wang, J. Zhang, B. Pan and Y. Xie, *J. Am. Chem. Soc.*, 2012, **135**, 18–21.

88 G. Li, H. Wang, X. Shi, C. Yang, R. Wang, B. He, J. Jin, Y. Gong, A. Tang and H. Yang, *Chem. Commun.*, 2022, **58**, 11276–11279.

89 Y. Wang, Y. Fan, D. Liao, Y. Wu, Y. Yu and C. Hu, *Energy Storage Mater.*, 2022, **51**, 212–222.

90 M. Yang, Z. Li, W. Chen, Y. Hu and Y. Yan, *Energy Fuels*, 2020, **34**, 8947–8955.

91 L. Wu, Y. Zhao, Y. Yu, B. Liao, H. Pang and H. Xie, *Inorg. Chem. Front.*, 2023, **10**, 651–665.

92 I. Janica, S. Del Buffa, A. Mikołajczak, M. Eredia, D. Pakulski, A. Ciesielski and P. Samorì, *Nanoscale*, 2018, **10**, 23182–23190.

93 F. Jia and S. Song, *Surf. Rev. Lett.*, 2014, **21**, 1430001.

94 Y. Zhou, A. M. LaChance, A. T. Smith, H. Cheng, Q. Liu and L. Sun, *Adv. Funct. Mater.*, 2019, **29**, 1807611.

95 L. A. Pérez-Maqueda, O. B. Caneo, J. Poyato and J. L. Pérez-Rodríguez, *Phys. Chem. Miner.*, 2001, **28**, 61–66.

96 J. B. Goodenough and Y. Kim, *J. Power Sources*, 2011, **196**, 6688–6694.

97 L. Zhang, X. Li, M. Yang and W. Chen, *Energy Storage Mater.*, 2021, **41**, 522–545.

98 H. Li, R. Y. Tay, S. H. Tsang, W. Liu and E. H. T. Teo, *Electrochim. Acta*, 2015, **166**, 197–205.

99 D. Jia, R. Tong, L. Ning, Z. Yang, Y. Zhang, W. Gu and X. Liu, *J. Alloys Compd.*, 2021, **857**, 157571.

100 C. Chowdhury, S. Karmakar and A. Datta, *ACS Energy Lett.*, 2016, **1**, 253–259.

101 M. Waqas, S. Ali, D. Chen, B. Boateng, Y. Han, M. Zhang, J. Han, J. B. Goodenough and W. He, *Composites, Part B*, 2019, **177**, 107448.

102 J. Bao, L. Zhu, H. Wang, S. Han, Y. Jin, G. Zhao, Y. Zhu, X. Guo, J. Hou, H. Yin and J. Tian, *J. Phys. Chem. C*, 2018, **122**, 23329–23335.

103 S. Kansara, S. K. Gupta, Y. Sonvane, M. V. Pajtler and R. Ahuja, *J. Phys. Chem. C*, 2019, **123**, 19340–19346.

104 M. Waqas, S. Ali, W. Lv, D. Chen, B. Boateng and W. He, *Adv. Mater. Interfaces*, 2019, **6**, 1801330.

105 D. Cao, Q. Zhang, A. M. Hafez, Y. Jiao, Y. Ma, H. Li, Z. Cheng, C. Niu and H. Zhu, *Small Methods*, 2019, **3**, 1800539.

106 S. Liu, J. Zhao, F. Li, Y. Zhao and G. Li, *J. Mater. Chem. A*, 2022, **10**, 5221–5229.

107 J. Wen, Y. Huang, J. Duan, Y. Wu, W. Luo, L. Zhou, C. Hu, L. Huang, X. Zheng, W. Yang, Z. Wen and Y. Huang, *ACS Nano*, 2019, **13**, 14549–14556.

108 L. Shi, A. Xu and T. Zhao, *ACS Appl. Mater. Interfaces*, 2017, **9**, 1987–1994.

109 K. Yan, H. W. Lee, T. Gao, G. Zheng, H. Yao, H. Wang, Z. Lu, Y. Zhou, Z. Liang, Z. Liu, S. Chu and Y. Cui, *Nano Lett.*, 2014, **14**, 6016–6022.

110 G. Li, H. Li, Y. Wang, D. Xiong, S. Wang, Y. Yan, S. Chen, B. Tian and Y. Shi, *ACS Appl. Mater. Interfaces*, 2021, **13**, 56109–56115.

111 S. Wang, L. Zhang, X. Cai, T. Chu, D. Liu, C. Han, X. Qin, F. Kang and B. Li, *J. Mater. Chem. A*, 2021, **9**, 25004–25012.

112 B. Shen, T. W. Zhang, Y. C. Yin, Z. X. Zhu, L. L. Lu, C. Ma, F. Zhou and H. B. Yao, *Chem. Commun.*, 2019, **55**, 7703–7706.

113 X. Fan, Y. Liu, J. Tan, S. Yang, X. Zhang, B. Liu, H. Cheng, Z. Sun and F. Li, *J. Mater. Chem. A*, 2022, **10**, 7653–7659.

114 W. Luo, L. Zhou, K. Fu, Z. Yang, J. Wan, M. Manno, Y. Yao, H. Zhu, B. Yang and L. Hu, *Nano Lett.*, 2015, **15**, 6149–6154.

115 Y. Liu, Y. Qiao, Y. Zhang, Z. Yang, T. Gao, D. Kirsch, B. Liu, J. Song, B. Yang and L. Hu, *Energy Storage Mater.*, 2018, **12**, 197–203.

116 J. Sheng, Q. Zhang, M. Liu, Z. Han, C. Li, C. Sun, B. Chen, X. Zhong, L. Qiu and G. Zhou, *Nano Lett.*, 2021, **21**, 8447–8454.

117 J. Wu, X. Li, Z. Rao, X. Xu, Z. Cheng, Y. Liao, L. Yuan, X. Xie, Z. Li and Y. Huang, *Nano Energy*, 2020, **72**, 104725.

118 J. Shim, H. J. Kim, B. G. Kim, Y. S. Kim, D.-G. Kim and J.-C. Lee, *Energy Environ. Sci.*, 2017, **10**, 1911–1916.

119 M. G. Rasul, M. Cheng, Y. Jiang, Y. Pan and R. Shahbazian-Yassar, *ACS Nanosci. Au*, 2022, **2**, 297–306.

120 Y. Zhao, Y. Qin, X. Da, X. Weng, Y. Gao, G. Gao, Y. Su and S. Ding, *ChemSusChem*, 2022, **15**, e202201554.

121 X. Zhang, W. Guo, L. Zhou, Q. Xu and Y. Min, *J. Mater. Chem. A*, 2021, **9**, 20530–20543.

122 Y. Li, L. Zhang, Z. Sun, G. Gao, S. Lu, M. Zhu, Y. Zhang, Z. Jia, C. Xiao, H. Bu, K. Xi and S. Ding, *J. Mater. Chem. A*, 2020, **8**, 9579–9589.

123 J. Yin, X. Xu, S. Jiang, Y. Lei and Y. Gao, *J. Power Sources*, 2022, **550**, 232139.

124 J. Li, L. Yang, H. Zhang and X. Ji, *Chem. Eng. J.*, 2022, **438**, 135418.

125 Z. Zhang, A. R. Gonzalez and K. L. Choy, *ACS Appl. Energy Mater.*, 2019, **2**, 7438–7448.

126 Q. Cheng, A. Li, N. Li, S. Li, A. Zangiabadi, T.-D. Li, W. Huang, A. C. Li, T. Jin, Q. Song, W. Xu, N. Ni, H. Zhai, M. Dontigny, K. Zaghib, X. Chuan, D. Su, K. Yan and Y. Yang, *Joule*, 2019, **3**, 1510–1522.

127 L. Zhu, Y. Wang, Y. Wu, W. Feng, Z. Liu, W. Tang, X. Wang and Y. Xia, *Adv. Funct. Mater.*, 2022, **32**, 2201136.

128 J.-H. Kim, D.-H. Park, J.-S. Jang, J.-H. Shin, M.-C. Kim, S.-B. Kim, S.-H. Moon, S.-N. Lee and K.-W. Park, *Chem. Eng. J.*, 2022, **446**, 137035.

129 Y. Zhao, L. Yang, J. Zhao, Q. Cai and P. Jin, *Phys. Chem. Chem. Phys.*, 2017, **19**, 18208–18216.

130 Y. Yi, H. Li, H. Chang, P. Yang, X. Tian, P. Liu, L. Qu, M. Li, B. Yang, H. Li, W. Zhu and S. Dai, *Chemistry*, 2019, **25**, 8112–8117.

131 D. Gao, Y. Li, Z. Guo, Z. Liu, K. Guo, Y. Fang, Y. Xue, Y. Huang and C. Tang, *J. Alloys Compd.*, 2021, **887**, 161273.

132 D. R. Deng, F. Xue, C. D. Bai, J. Lei, R. Yuan, M. S. Zheng and Q. F. Dong, *ACS Nano*, 2018, **12**, 11120–11129.

133 Y. Fan, Z. Yang, W. Hua, D. Liu, T. Tao, M. M. Rahman, W. Lei, S. Huang and Y. Chen, *Adv. Energy Mater.*, 2017, **7**, 1602380.

134 Y. Mussa, Z. Bayhan, N. Althubaiti, M. Arsalan and E. Alsharaeh, *Mater. Chem. Phys.*, 2021, **257**, 123807.

135 W. Gao, Y. Liu, C. Cao, Y. Zhang, Y. Xue and C. Tang, *J. Colloid Interface Sci.*, 2022, **610**, 527–537.

136 B. He, W.-C. Li, Y. Zhang, X.-F. Yu, B. Zhang, F. Li and A.-H. Lu, *J. Mater. Chem. A*, 2018, **6**, 24194–24200.

137 K. Zhu, P. Xue, G. Cheng, M. Wang, H. Wang, C. Bao, K. Zhang, Q. Li, J. Sun, S. Guo, Y. Yao and C.-P. Wong, *Energy Storage Mater.*, 2021, **43**, 130–142.

138 H. S. Kim, H. J. Kang, H. Lim, H. J. Hwang, J. W. Park, T. G. Lee, S. Y. Cho, S. G. Jang and Y. S. Jun, *Nanomaterials*, 2021, **12**, 11.

139 P. J. H. Kim, J. Seo, K. Fu, J. Choi, Z. Liu, J. Kwon, L. Hu and U. Paik, *NPG Asia Mater.*, 2017, **9**, e375.

140 Y. Fan, D. Liu, M. M. Rahman, T. Tao, W. Lei, S. Mateti, B. Yu, J. Wang, C. Yang and Y. Chen, *ACS Appl. Energy Mater.*, 2019, **2**, 2620–2628.

141 J. Zhang, W. Ma, Z. Feng, F. Wu, D. Wei, B. Xi and S. Xiong, *J. Energy Chem.*, 2019, **39**, 54–60.

142 T. Wu, T. Yang, J. Zhang, X. Zheng, K. Liu, C. Wang and M. Chen, *J. Energy Chem.*, 2021, **59**, 220–228.

143 X. Xu, L. Wang, H. Fei and L. Ci, *J. Mater. Sci.: Mater. Electron.*, 2019, **30**, 19119–19125.

144 X. Yin, L. Wang, Y. Kim, N. Ding, J. Kong, D. Safanama, Y. Zheng, J. Xu, D. V. M. Repaka, K. Hippalgaonkar, S. W. Lee, S. Adams and G. W. Zheng, *Adv. Sci.*, 2020, **7**, 2001303.

145 D. Adekoya, S. Zhang and M. Hankel, *Carbon*, 2021, **176**, 480–487.

146 Y. Qian, H. Lai, J. Ma, G. Deng, B. Long, T. Song, L. Liu, X. Wang and Y. Tong, *J. Colloid Interface Sci.*, 2022, **606**, 537–543.

147 K. Liu, J. Man, J. Cui, H. Zhang, T. Li, J. Yang, Z. Wen and J. Sun, *Mater. Lett.*, 2019, **234**, 117–120.

148 J. Xu, Y. Xu, G. Tang, H. Tang and H. Jiang, *Appl. Surf. Sci.*, 2019, **492**, 37–44.

149 H. Tran Huu, X. D. Nguyen Thi, K. Nguyen Van, S. J. Kim and V. Vo, *Materials*, 2019, **12**, 1730.

150 D. Versaci, J. Amici, C. Francia and S. Bodoardo, *Solid State Ionics*, 2020, **346**, 115210.

151 Y. Zuo, X. Xu, C. Zhang, J. Li, R. Du, X. Wang, X. Han, J. Arbiol, J. Llorca, J. Liu and A. Cabot, *Electrochim. Acta*, 2020, **349**, 136369.

152 D. D. Pathak, D. P. Dutta, B. R. Ravuri, A. Ballal, A. C. Joshi and A. K. Tyagi, *Electrochim. Acta*, 2021, **370**, 137715.

153 H. Tran Huu, H. T. T. Le, T. Huong Nguyen, L. Nguyen Thi, V. Vo and W. Bin Im, *Appl. Surf. Sci.*, 2021, **549**, 149312.

154 V. Vo, X. D. Nguyen Thi, Y.-S. Jin, G. Ly Thi, T. T. Nguyen, T. Q. Duong and S.-J. Kim, *Chem. Phys. Lett.*, 2017, **674**, 42–47.

155 H. H. Tran, P. H. Nguyen, V. H. Cao, L. T. Nguyen, V. M. Tran, M. L. Phung Le, S.-J. Kim and V. Vo, *Chem. Phys. Lett.*, 2019, **715**, 284–292.

156 Q. D. Le, P. N. Ngoc, H. T. Huu, T. H. T. Nguyen, T. N. Van, L. N. Thi, M. K. Le, V. M. Tran, M. L. P. Le and V. Vo, *Chem. Phys. Lett.*, 2022, **796**, 139550.

157 Y. Liu, S. He, Y. Zhong, X. Xu and Z. Shao, *J. Alloys Compd.*, 2019, **805**, 522–530.

158 H. S. H. Mohamed, C.-F. Li, L. Wu, W.-H. Shi, W.-D. Dong, J. Liu, Z.-Y. Hu, L.-H. Chen, Y. Li and B.-L. Su, *Chem. Eng. J.*, 2021, **407**, 126941.

159 P. Zhang, B. Cai, Y. Feng, H. Pan and J. Yao, *J. Alloys Compd.*, 2021, **875**, 160077.

160 H. Xu, L. Sun, W. Li, M. Gao, Q. Zhou, P. Li, S. Yang and J. Lin, *Chem. Eng. J.*, 2022, **435**, 135129.

161 S. Wang, Y. Shi, C. Fan, J. Liu, Y. Li, X. L. Wu, H. Xie, J. Zhang and H. Sun, *ACS Appl. Mater. Interfaces*, 2018, **10**, 30330–30336.

162 W. Kong, J. Yu, X. Shi, J. Yin, H. Yang and Z. Wen, *J. Electrochem. Soc.*, 2020, **167**, 060518.

163 S. Kang, X. Li, C. Yin, J. Wang, M. S. Aslam, H. Qi, Y. Cao, J. Jin and L. Cui, *J. Colloid Interface Sci.*, 2019, **554**, 269–277.

164 H. Zhang, J. Yin, Y. Liu, Z. Lang, Y. Liu, W. He, L. Ma, J. Cui and J. Sun, *J. Electroanal. Chem.*, 2020, **862**, 114004.

165 H. Zuhaib, M. Munisamy, N. Perumal, H.-W. Yang, W. S. Kang and S.-J. Kim, *Mater. Chem. Phys.*, 2023, **298**, 127463.

166 L. Wan, Y. Tang, L. Chen, K. Wang, J. Zhang, Y. Gao, J. Y. Lee, T. Lu, X. Xu, J. Li, Y. Zheng and L. Pan, *Chem. Eng. J.*, 2021, **410**, 128349.

167 G. M. Weng, Y. Xie, H. Wang, C. Karpovich, J. Lipton, J. Zhu, J. Kong, L. D. Pfefferle and A. D. Taylor, *Angew. Chem., Int. Ed.*, 2019, **58**, 13727–13733.

168 K. Sun, Y. Wang, C. Chang, S. Yang, S. Di, P. Niu, S. Wang and L. Li, *Chem. Eng. J.*, 2021, **425**, 131591.

169 H. Shi, S. Wang, Y. Xia, X. Yan, D. Wang, Y. Yin, P. Huai, Z. Xu, C. Min, S. Liu and X. Wu, *ACS Appl. Energy Mater.*, 2022, **5**, 7308–7316.

170 H. L. Tran Huu, H. T. T. Nguyen, T. Huong Nguyen Thi, L. Vo, V. Im and W. Bin, *Int. J. Energy Res.*, 2021, **46**, 3233–3248.

171 D. Adekoya, M. Li, M. Hankel, C. Lai, M.-S. Balogun, Y. Tong and S. Zhang, *Energy Storage Mater.*, 2020, **25**, 495–501.

172 J. Wu, L. Tian, H. Duan, Y. Cheng and L. Shi, *ACS Appl. Mater. Interfaces*, 2021, **13**, 46821–46829.

173 Y. Jeon, S. Kang, S. H. Joo, M. Cho, S. O. Park, N. Liu, S. K. Kwak, H.-W. Lee and H.-K. Song, *Energy Storage Mater.*, 2020, **31**, 505–514.

174 Z. Lu, Q. Liang, B. Wang, Y. Tao, Y. Zhao, W. Lv, D. Liu, C. Zhang, Z. Weng, J. Liang, H. Li and Q.-H. Yang, *Adv. Energy Mater.*, 2019, **9**, 1803186.

175 W. Lu, H. Yang, J. Chen, C. Sun and F. Li, *Sci. China: Mater.*, 2021, **64**, 2675–2682.

176 Y. Xu, T. Li, L. Wang and Y. Kang, *Adv. Mater.*, 2019, **31**, e1901662.

177 Y. Roh, J. Song, J.-H. Lee, H. Kwon, J. Baek, D. Shin, Y. G. Yoo, S. Ha, W. Kim, K. Ryu and H.-T. Kim, *Energy Storage Mater.*, 2022, **51**, 777–788.

178 J. Wang, Z. Meng, W. Yang, X. Yan, R. Guo and W. Q. Han, *ACS Appl. Mater. Interfaces*, 2019, **11**, 819–827.

179 Z. Zhuang, B. Ju, P. Ma, L. Yang and F. Tu, *Ionics*, 2021, **27**, 1069–1079.

180 F. Zhao, P. Zhai, Y. Wei, Z. Yang, Q. Chen, J. Zuo, X. Gu and Y. Gong, *Adv. Sci.*, 2022, **9**, e2103930.

181 H. Zhang, Y. Wang, S. Ju, P. Gao, T. Zou, T. Zhang, J. Wang, G. Xia and X. Yu, *Energy Storage Mater.*, 2022, **52**, 220–229.

182 X. Luan, C. Wang, C. Wang, X. Gu, J. Yang and Y. Qian, *ACS Appl. Mater. Interfaces*, 2020, **12**, 11265–11272.

183 J. Hu, J. Tian and C. Li, *ACS Appl. Mater. Interfaces*, 2017, **9**, 11615–11625.

184 J. Li, L. Zhu, H. Xie, W. Zheng and K. Zhang, *Colloids Surf., A*, 2023, **657**, 130520.

185 Q. Zhang, Q. Wang, S. Huang, Y. Jiang and Z. Chen, *Inorg. Chem. Commun.*, 2021, **131**, 108793.

186 X. Hao, K. Chen, Y. Tang, X. Zhong and K. Cai, *J. Alloys Compd.*, 2023, **942**, 169064.

187 H. Liang, S. Wang, Q. Ye, C. Zeng, Z. Tong, Y. Ma and H. Li, *Chem. Commun.*, 2022, **58**, 10821–10824.

188 J. Wei, X. Zheng, W. Lin, Y. Si, K. Ji, C. Wang and M. Chen, *J. Alloys Compd.*, 2022, **909**, 164825.

189 Y. Huang, B. Chen, J. Duan, F. Yang, T. Wang, Z. Wang, W. Yang, C. Hu, W. Luo and Y. Huang, *Angew. Chem., Int. Ed.*, 2020, **59**, 3699–3704.

190 Z. Guo, C. Ye, T. Zhao, W. Wu, W. Kou, Y. Zhang, W. Dong, W. Li and J. Wang, *J. Power Sources*, 2023, **562**, 232784.

191 Q. Pang and L. F. Nazar, *ACS Nano*, 2016, **10**, 4111–4118.

192 Q. Pang, X. Liang, C. Y. Kwok, J. Kulisch and L. F. Nazar, *Adv. Energy Mater.*, 2016, **7**, 1601630.

193 Y. Zheng, H. Li, H. Yuan, H. Fan, W. Li and J. Zhang, *Appl. Surf. Sci.*, 2018, **434**, 596–603.

194 Y. Gong, C. Fu, G. Zhang, H. Zhou and Y. Kuang, *Electrochim. Acta*, 2017, **256**, 1–9.

195 J. Zhang, J.-Y. Li, W.-P. Wang, X.-H. Zhang, X.-H. Tan, W.-G. Chu and Y.-G. Guo, *Adv. Energy Mater.*, 2018, **8**, 1702839.

196 Z. Jia, H. Zhang, Y. Yu, Y. Chen, J. Yan, X. Li and H. Zhang, *J. Energy Chem.*, 2020, **43**, 71–77.

197 L. Qu, P. Liu, Y. Yi, T. Wang, P. Yang, X. Tian, M. Li, B. Yang and S. Dai, *ChemSusChem*, 2019, **12**, 213–223.

198 P. Song, Z. Chen, Y. Chen, Q. Ma, X. Xia and H. Liu, *Electrochim. Acta*, 2020, **363**, 137217.

199 X. Wang, G. Li, M. Li, R. Liu, H. Li, T. Li, M. Sun, Y. Deng, M. Feng and Z. Chen, *J. Energy Chem.*, 2021, **53**, 234–240.

200 Y. Li, M. Chen, P. Zeng, H. Liu, H. Yu, Z. Luo, Y. Wang, B. Chang and X. Wang, *J. Alloys Compd.*, 2021, **873**, 159883.

201 H. Pan, X. Huang, C. Wang, D. Liu, D. Wang, R. Zhang, S. Li, C. Lv, L. Zhao, J. Wang and X. Huang, *Chem. Eng. J.*, 2021, **410**, 128424.

202 S.-H. Moon, J.-H. Shin, J.-H. Kim, J.-S. Jang, S.-B. Kim, Y.-Y. Park, S.-N. Lee and K.-W. Park, *Mater. Chem. Phys.*, 2022, **287**, 126267.

203 H. Zhang, X. Lin, J. Li, T. Han, M. Zhu, X. Xu, C. Hu and J. Liu, *J. Alloys Compd.*, 2021, **881**, 160629.

204 G. Xu, L. Li, M. Li, C. Xi, J. Yan, R. Li, Y. Chao, C. Yang and Y. Yu, *Appl. Surf. Sci.*, 2022, **604**, 154556.

205 E. Abd-Alkuder Salman, K. Abaid Samawi, M. Fawzi Nassar, G. Abdulkareem-Alsultan and E. Abdulmalek, *J. Electroanal. Chem.*, 2023, **945**, 117629.

206 W.-W. Liu, S.-T. Niu, Z.-Q. Xu, R. Zou, C.-Y. Cui, Y.-X. Lei, X.-B. Zhang and F. Ran, *Appl. Surf. Sci.*, 2023, **609**, 155327.

207 S. Majumder, M. Shao, Y. Deng and G. Chen, *J. Power Sources*, 2019, **431**, 93–104.

208 H. Zou, Y. Zou, Y. Lv, Z. Ao, N. Chen and Y. Huang, *ACS Appl. Energy Mater.*, 2022, **5**, 10067–10075.

209 M. Chen, X. Zhao, Y. Li, P. Zeng, H. Liu, H. Yu, M. Wu, Z. Li, D. Shao, C. Miao, G. Chen, H. Shu, Y. Pei and X. Wang, *Chem. Eng. J.*, 2020, **385**, 123905.

210 Y. Wang, L. Yang, Y. Chen, Q. Li, C. Chen, B. Zhong, X. Guo, Z. Wu and G. Wang, *ACS Appl. Mater. Interfaces*, 2020, **12**, 57859–57869.

211 M. Luo, Y. Bai, R. Sun, Z. Wang, W. Sun, P. Lin, X. Dai and K. Sun, *Ind. Eng. Chem. Res.*, 2021, **60**, 1231–1240.

212 W. B. Luo, S. L. Chou, J. Z. Wang, Y. C. Zhai and H. K. Liu, *Small*, 2015, **11**, 2817–2824.

213 Q. Liu and J. Zhang, *Langmuir*, 2013, **29**, 3821–3828.

214 M.-Q. Wang, W.-H. Yang, H.-H. Wang, C. Chen, Z.-Y. Zhou and S.-G. Sun, *ACS Catal.*, 2014, **4**, 3928–3936.

215 X. Zou, J. Su, R. Silva, A. Goswami, B. R. Sathe and T. Asefa, *Chem. Commun.*, 2013, **49**, 7522–7524.

216 Y. Wu, T. Wang, Y. Zhang, S. Xin, X. He, D. Zhang and J. Shui, *Sci. Rep.*, 2016, **6**, 24314.

217 X. Li, Y. Zhao, L. Ding, D. Wang, Q. Guo, Z. Li, H. Luo, D. Zhang and Y. Yu, *Nanomaterials*, 2021, **11**, 1088.

218 W. Zhao, J. Wang, R. Yin, B. Li, X. Huang, L. Zhao and L. Qian, *J. Colloid Interface Sci.*, 2020, **564**, 28–36.

219 R. Cao, Y. Cui, G. Huang, W. Liu, J. Liu and X. Zhang, *Nano Res.*, 2023, **16**, 8405–8410.

220 E. Lokcu, N. Kacar, M. Cayirli, R. C. Ozden and M. Anik, *ACS Appl. Mater. Interfaces*, 2022, **14**, 34583–34592.

221 W. Chen, T. Lei, W. Lv, Y. Hu, Y. Yan, Y. Jiao, W. He, Z. Li, C. Yan and J. Xiong, *Adv. Mater.*, 2018, e1804084.

222 C. Chen, Y. Ma and C. Wang, *Sustainable Mater. Technol.*, 2019, **19**, e00086.

223 M. S. Chen, W. Fu, Y. Hu, M. Y. Chen, Y. J. Chiou, H. M. Lin, M. Zhang and Z. Shen, *Nanoscale*, 2020, **12**, 16262–16269.

224 M. L. Para, D. Versaci, J. Amici, M. F. Caballero, M. V. Cozzarin, C. Francia, S. Bodoardo and M. Gamba, *J. Electroanal. Chem.*, 2021, **880**, 114876.

225 P. Xu, X. Yan, Y. Zhou, C. Wang, H. Cheng and Y. Zhang, *Soft Matter*, 2022, **18**, 2522–2527.

226 J. Nunes-Pereira, A. C. Lopes, C. M. Costa, R. Leones, M. M. Silva and S. Lanceros-Méndez, *Electroanalysis*, 2012, **24**, 2147–2156.

227 M. Raja, T. P. Kumar, G. Sanjeev, L. Zolin, C. Gerbaldi and A. M. Stephan, *Ionics*, 2014, **20**, 943–948.

228 C. Fang, S. Yang, X. Zhao, P. Du and J. Xiong, *Mater. Res. Bull.*, 2016, **79**, 1–7.

229 M. Carter, M. H. Parekh, V. Tomar, J. E. Dietz and V. G. Pol, *Appl. Clay Sci.*, 2021, **208**, 106111.

230 Y. Yang, B. Yang, M. Luo, Y. Yang, Y. Wang, J. Miao, S. Wang, Z. Zheng, J. Qian, R. Xia, Y. Ke and Y. Tu, *Electrochim. Acta*, 2023, **446**, 142074.

231 M. Wang, F. Zhao, Z. Guo and S. Dong, *Electrochim. Acta*, 2004, **49**, 3595–3602.

232 S. Kim and S.-J. Park, *Solid State Ionics*, 2007, **178**, 973–979.

233 S. Kim, E.-J. Hwang, Y. Jung, M. Han and S.-J. Park, *Colloids Surf., A*, 2008, **313–314**, 216–219.

234 H. Zhao, W. Kang, N. Deng, M. Liu and B. Cheng, *Chem. Eng. J.*, 2020, **384**, 123312.

235 M. Wang, Y. Li, S.-Y. Li, X.-X. Jia, B. Nie, H.-T. Sun, Y.-Y. Wang and J. Zhu, *Rare Met.*, 2023, **42**, 2157–2165.

236 Q. Ma, X. Sun, P. Liu, Y. Xia, X. Liu and J. Luo, *Angew. Chem., Int. Ed.*, 2019, **58**, 6200–6206.

237 Y. Feng, B. Zhong, R. Zhang, M. Peng, Z. Hu, Z. Wu, N. Deng, W. Zhang and K. Zhang, *Adv. Energy Mater.*, 2023, **13**, 2203912.

238 W. Wang, Y. Yang, H. Luo and J. Zhang, *J. Colloid Interface Sci.*, 2022, **614**, 593–602.

239 F. Wu, H. Lv, S. Chen, S. Lorger, V. Srot, M. Oschatz, P. A. van Aken, X. Wu, J. Maier and Y. Yu, *Adv. Funct. Mater.*, 2019, **27**, 1902820.

240 Y. Nan, S. Li, C. Han, H. Yan, Y. Ma, J. Liu, S. Yang and B. Li, *Adv. Funct. Mater.*, 2021, **31**, 2102336.

241 T. Zeng, Y. Yan, M. He, D. Du, X. Wen, B. Zhou and C. Shu, *J. Mater. Chem. A*, 2022, **10**, 23712–23721.

242 X.-Q. Xu, F.-N. Jiang, S.-J. Yang, Y. Xiao, H. Liu, F. Liu, L. Liu and X.-B. Cheng, *J. Energy Chem.*, 2022, **69**, 205–210.

243 J. Zhao, D. Chen, B. Boateng, G. Zeng, Y. Han, C. Zhen, J. B. Goodenough and W. He, *J. Power Sources*, 2020, **451**, 227773.

244 M. Yang, N. Jue, Y. Chen and Y. Wang, *Nanoscale Res. Lett.*, 2021, **16**, 52.

245 Y. Zhai, X. Wang, Y. Chen, X. Sang, H. Liu, J. Sheng, Y. Wu, X. Wang and L. Li, *J. Membr. Sci.*, 2021, **621**, 118996.

246 L. Pan, H. He and H. He, *Mater. Today Energy*, 2022, **26**, 101015.

247 W. Chen, Y. Hu, W. Lv, T. Lei, X. Wang, Z. Li, M. Zhang, J. Huang, X. Du, Y. Yan, W. He, C. Liu, M. Liao, W. Zhang, J. Xiong and C. Yan, *Nat. Commun.*, 2019, **10**, 4973.

248 Y. M. Jeon, S. Kim, M. Lee, W. B. Lee and J. H. Park, *Adv. Energy Mater.*, 2020, **10**, 2003114.

249 Y. Wang, X. Li, Y. Qin, D. Zhang, Z. Song and S. Ding, *Nano Energy*, 2021, **90**, 106490.

250 H. Porthault, C. Calberg, J. Amiran, S. Martin, C. Páez, N. Job, B. Heinrichs, D. Liquet and R. Salot, *J. Power Sources*, 2021, **482**, 229055.

251 W. Y. Li, Z. H. Luo, X. Long, J. Y. Long, C. Pang, H. Li, X. Zhi, B. Shi, J. J. Shao and Y. B. He, *ACS Appl. Mater. Interfaces*, 2021, **13**, 51107–51116.

252 W. Tang, S. Tang, X. Guan, X. Zhang, Q. Xiang and J. Luo, *Adv. Funct. Mater.*, 2019, **29**, 1900648.

253 Y. Zhang, J. Huang, H. Liu, W. Kou, Y. Dai, W. Dang, W. Wu, J. Wang, Y. Fu and Z. Jiang, *Adv. Energy Mater.*, 2023, **13**, 2300156.

254 W. Ahn, S. N. Lim, D. U. Lee, K.-B. Kim, Z. Chen and S.-H. Yeon, *J. Mater. Chem. A*, 2015, **3**, 9461–9467.

255 Y. Yang, G. Meng, H. Wang, W. Wang and J. Zhang, *Chem. Eng. J.*, 2023, **451**, 138914.

256 X. Long, Z.-H. Luo, W.-H. Zhou, S.-K. Zhu, Y. Song, H. Li, C.-N. Geng, B. Shi, Z.-Y. Han, G.-M. Zhou, W. Lv and J.-J. Shao, *Energy Storage Mater.*, 2022, **52**, 120–129.

257 M. Yang, J. Nan, W. Chen, A. Hu, H. Sun, Y. Chen and C. Wu, *Electrochem. Commun.*, 2021, **125**, 106971.

258 W. Wang, K. Xi, B. Li, H. Li, S. Liu, J. Wang, H. Zhao, H. Li, A. M. Abdelkader, X. Gao and G. Li, *Adv. Energy Mater.*, 2022, **12**, 2200160.

259 R. Xu, Y. Sun, Y. Wang, J. Huang and Q. Zhang, *Chin. Chem. Lett.*, 2017, **28**, 2235–2238.

260 P. Zhai, N. Peng, Z. Sun, W. Wu, W. Kou, G. Cui, K. Zhao and J. Wang, *J. Mater. Chem. A*, 2020, **8**, 23344–23353.

261 M. Xie, L. Li, K. Yuan, Y. Ma and B. Liu, *J. Mater. Sci.: Mater. Electron.*, 2018, **30**, 2030–2036.

262 Z. Xiao, R. Wang, D. Jiang, Z. Qian, Y. Li, K. Yang, Y. Sun, Z. Zeng and F. Wu, *ACS Appl. Energy Mater.*, 2021, **4**, 7440–7461.

263 M. G. Rasul, A. Kiziltas, B. Arfaei and R. Shahbazian-Yassar, *npj 2D Mater. Appl.*, 2021, **5**, 56.

264 S. A. Thomas, M. R. Pallavolu, M. E. Khan and J. Cherusseri, *J. Energy Storage*, 2023, **68**, 107673.

265 L. Wu, X. He, Y. Zhao, K. Huang, Z. Tong, B. Liao and H. Pang, *Green Chem.*, 2024, **26**, 678–704.